Monthly Notices
of the
ROYAL ASTRONOMICAL SOCIETY

MNRAS **517,** 2801–2817 (2022) https://doi.org/10.1093/mnras/stac2700
Advance Access publication 2022 September 24

Radio observations of the Black Hole X-ray Binary EXO 1846−031 re-awakening from a 34-year slumber

D. R. A. Williams,[1,2]★ S. E. Motta,[2,3] R. Fender,[2,4] J. C. A. Miller-Jones,[5] J. Neilsen,[6] J. R. Allison,[7,2] J. Bright,[2,8] I. Heywood,[2,9] P. F. L. Jacob,[2] L. Rhodes,[2,10] E. Tremou,[11] P. A. Woudt,[4] J. van den Eijnden,[2] F. Carotenuto,[2] D. A. Green,[12] D. Titterington,[12] A. J. van der Horst[13,14] and P. Saikia[15]

[1]*Jodrell Bank Centre for Astrophysics, School of Physics and Astronomy, The University of Manchester, Manchester, M13 9PL, UK*
[2]*Department of Physics, University of Oxford, Denys Wilkinson Building, Keble Road, Oxford, OX1 3RH, UK*
[3]*Istituto Nazionale di Astrofisica, Osservatorio Astronomico di Brera, via E. Bianchi 46, I-23807 Merate (LC), Italy*
[4]*Department of Astronomy, University of Cape Town, Private Bag X3, Rondebosch 7701, South Africa*
[5]*International Centre for Radio Astronomy Research - Curtin University, Perth, Western Australia 6845, Australia*
[6]*Department of Physics, Villanova University, Mendel Science Center, Villanova PA, 19085, USA*
[7]*First Light Fusion Ltd., Unit 9/10 Oxford Industrial Park, Mead Road, Yarnton, Kidlington OX5 1QU, UK*
[8]*Center for Interdisciplinary Exploration and Research in Astrophysics (CIERA) and Department of Physics and Astronomy, Northwestern University, Evanston, IL 60208, USA*
[9]*Department of Physics and Electronics, Rhodes University, PO Box 94, Grahamstown 6140, South Africa*
[10]*Max-Planck-Institut für Radioastronomie, Auf dem Hügel 69, D-53121 Bonn, Germany*
[11]*National Radio Astronomy Observatory, Socorro, NM 87801, USA*
[12]*Astrophysics Group, Cavendish Laboratory, 19 J. J. Thomson Avenue, Cambridge CB3 0HE, UK*
[13]*Department of Physics, The George Washington University, 725 21st Street NW, Washington, DC 20052, USA*
[14]*Astronomy, Physics, and Statistics Institute of Sciences (APSIS), 725 21st Street NW, Washington, DC 20052, USA*
[15]*Center for Astro, Particle and Planetary Physics (CAP^3), New York University Abu Dhabi, PO Box 129188, Abu Dhabi, UAE*

Accepted 2022 September 18. Received 2022 September 12; in original form 2022 May 23

ABSTRACT

We present radio [1.3 GHz MeerKAT, 4–8 GHz Karl G. Jansky Very Large Array (VLA), and 15.5 GHz Arcminute Microkelvin Imager Large Array (AMI-LA)] and X-ray (*Swift* and *MAXI*) data from the 2019 outburst of the candidate Black Hole X-ray Binary (BHXB) EXO 1846−031. We compute a Hardness–Intensity diagram, which shows the characteristic q-shaped hysteresis of BHXBs in outburst. EXO 1846−031 was monitored weekly with MeerKAT and approximately daily with AMI-LA. The VLA observations provide sub-arcsecond-resolution images at key points in the outburst, showing moving radio components. The radio and X-ray light curves broadly follow each other, showing a peak on ∼MJD 58702, followed by a short decline before a second peak between ∼MJD 58731–58739. We estimate the minimum energy of these radio flares from equipartition, calculating values of $E_{\rm min} \sim 4 \times 10^{41}$ and 5×10^{42} erg, respectively. The exact date of the return to 'quiescence' is missed in the X-ray and radio observations, but we suggest that it likely occurred between MJD 58887 and 58905. From the *Swift* X-ray flux on MJD 58905 and assuming the soft-to-hard transition happened at 0.3–3 per cent Eddington, we calculate a distance range of 2.4–7.5 kpc. We computed the radio:X-ray plane for EXO 1846−031 in the 'hard' state, showing that it is most likely a 'radio-quiet' BH, preferentially at 4.5 kpc. Using this distance and a jet inclination angle of $\theta = 73^{\circ}$, the VLA data place limits on the intrinsic jet speed of $\beta_{\rm int} = 0.29c$, indicating subluminal jet motion.

Key words: radio continuum: transients – X-rays: binaries – X-rays: individual: EXO 1846−031.

1 INTRODUCTION

X-ray binaries (XBs) are binary systems which contain a compact object, such as a neutron star (NS) or black hole (BH), where matter is transferred from a secondary, non-degenerate donor star, via an accretion disc around the compact object. The majority of BHXBs spend most of their lives in a '*quiescent*' state, accreting at low rates and undetectable in the X-rays for years to decades. BHXBs are commonly discovered when they enter an '*outburst*'; their multiband flux increases by many orders of magnitude as the accretion rate increases. Usually, after weeks to months, the BHXB will gradually transition from the 'hard' power-law ($\Gamma \sim 1.5$) dominated state into a 'soft' state (see, Remillard & McClintock 2006; Belloni & Motta 2016, for full descriptions of different X-ray spectral states), whereby the X-ray spectrum gradually becomes dominated by blackbody disc emission and the X-ray flux begins to decrease, through 'intermediate' states (see e.g. Homan & Belloni

---

★ E-mail: david.williams-7@manchester.ac.uk

2005). The intermediate states are defined by their X-ray timing and spectral characteristics. They can be rapid, sometimes lasting only hours (Belloni et al. 2006). After weeks to months in the 'soft' state, the BHXB moves back to the 'hard' state at 0.3–3 per cent of the Eddington luminosity (Maccarone 2003; Kalemci et al. 2013; Vahdat Motlagh, Kalemci & Maccarone 2019), before fading back into quiescence. This hysteresis is best demonstrated on a 'Hardness–Intensity Diagram' (HID), whereby the X-ray flux (or luminosity) is plotted against the X-ray spectral hardness (e.g. Fender, Belloni & Gallo 2004).

The different X-ray states are closely associated with radio properties of BHXBs (Corbel et al. 2000; Fender & Belloni 2004; Fender et al. 2004). During the 'hard' state (and quiescence), a flat-spectrum ($S \propto \nu^{\alpha}$, with spectral index $\alpha \sim 0$), steady jet persists and is observed (e.g. Cygnus X-1, Stirling et al. 2001). When a BHXB transitions out of the 'hard' state, the steady jet is quenched by at least two orders of magnitude (Coriat et al. 2011; Russell et al. 2011, 2019). Transient ejecta can be emitted from the BHXB as the source passes through the 'intermediate' states (Miller-Jones et al. 2012; Russell et al. 2019; Wood et al. 2021), which may be associated with bright radio flares as a signature of the ejection (Corbel et al. 2004; Fender et al. 2004). These radio ejecta can be tracked as they move away from the BHXB and interact with the interstellar medium (Mirabel & Rodríguez 1994; Corbel et al. 2002, 2005; Bright et al. 2020; Carotenuto et al. 2021). Transient radio ejecta typically show radio spectral indices which steepen ($\alpha < 0$) over time as the component expands and becomes optically-thin. If the distance is known, observations of BHXB radio jets can enable the calculation of fundamental properties of the jet and BH system (Mirabel & Rodríguez 1994; Fender 2006). The steady jet only reappears when the source transitions back into the 'hard' state and into quiescence.

During the X-ray 'hard' state, the radio and X-ray behaviour of BHXBs is correlated and has been studied in depth for many sources using quasi-simultaneous observations (e.g. Corbel et al. 2003; Gallo, Fender & Pooley 2003; Coriat et al. 2011; Corbel et al. 2013), and is known as the radio:X-ray plane. It was thought that all XBs followed a relation in the form of $L_{\rm Radio} \propto L_{\rm X-ray}^{0.6}$, based upon early observations of GX 339−4 (Hannikainen et al. 1998; Gallo et al. 2003; Corbel et al. 2003, 2013). This relation extends down to very low luminosities, i.e. into quiescence (Corbel et al. 2003, 2013; Plotkin et al. 2017; Tremou et al. 2020), and has been observed in other sources such as V404 Cygni (e.g. Corbel, Koerding & Kaaret 2008) and XTE J1118+480 (Gallo et al. 2014). However, further observations revealed the presence of another population of BHXBs which are less radio luminous than this relation, a so-called 'radio-quiet' branch, which followed $L_{\rm R} \propto L_{\rm X}^{1.4}$, such as H 1743−322 (e.g. Coriat et al. 2011; Williams et al. 2020). In some of these 'radio-quiet' objects, they are then found to re-join the 'radio-loud' branch when they go back into quiescence (Coriat et al. 2011; Carotenuto et al. 2021). The underlying cause of the split tracks (see Gallo, Miller & Fender 2012; Gallo et al. 2014; Gallo, Degenaar & van den Eijnden 2018, for a clustering analysis into the statistical robustness of this split) for BHXBs is not known, but it may be due to differences in the radiative efficiency of the accretion flow (Coriat et al. 2011; Koljonen & Russell 2019), an inclination effect of the source (Motta, Casella & Fender 2018), differences in the accretion disc contribution (Meyer-Hofmeister & Meyer 2014) or changes in the magnetic field (Casella & Pe'er 2009). For the purposes of this paper, we will refer to the original $L_{\rm R} \propto L_{\rm X}^{0.6}$ correlation sources as 'radio-loud' objects, and those that diverge on to the $L_{\rm R} \propto L_{\rm X}^{1.4}$ track as 'radio-quiet' sources.

In this work, we investigate the 2019 outburst of the historical X-ray transient EXO 1846−031. EXO 1846−031 was first discovered as an 'ultra-soft X-ray transient' by the *EXOSAT* satellite during slewing manoeuvres on 1985 April 3 (Parmar & White 1985). Subsequent targeted *EXOSAT* observations, optical and radio observations were performed, the results of which we summarize below: (i) the X-ray properties indicated EXO 1846−031 was a BH candidate (Parmar et al. 1993); (ii) the EXO 1846−031 field is crowded in the X-rays (Parmar et al. 1993) and heavily confused in the radio (Nelson & Spencer 1988); (iii) there is a large absorption along the line-of-sight, $N_{\rm H} \sim 3.5 \times 10^{22}$ atoms cm^{-2} (Parmar et al. 1993); iv) no optical counterpart was found to a limiting magnitude of 21.5 mag (Wenzel & Huth 1985; Gottwald et al. 1991; Zhang et al. 1994); v) the distance is crudely estimated to be ∼7 kpc from scaling the first *EXOSAT* observation peak flux to a luminosity of 10^{38} erg s^{-1} (Parmar et al. 1993).

Given the large number of unknown parameters of EXO 1846−031, the study of further outbursts is key for constraining the system properties. Despite reports of a possible outburst in 1994 (Inoue et al. 1994; Zhang et al. 1994), no new bona-fide outbursts of EXO 1846−031 had been reported until 2019 July 31 (Negoro et al. 2019). On MJD 58687.864 (2019 July 23 20:44 UTC), the nova alert system on-board the *MAXI/GSC* satellite had detected an increase in X-ray flux from the region around a nearby source IGR J18483−0311 (Negoro et al. 2019), but it was only realized a week later on MJD 58694.878 (2019 July 30 21:05 UTC) that the source of the flux increase was instead EXO 1846−031 re-awakening from a ∼34 year slumber. Following an increase in the 2–4 and 4–10 keV fluxes seen by *MAXI/GSC*, EXO 1846−031 was confirmed to be in the 'hard' state and in outburst (Negoro et al. 2019). A further observation with the X-ray telescope (XRT) instrument onboard the Neil Gehrels *Swift* Observatory gave an improved localization ($18^{\rm h}49^{\rm m}16\overset{\rm s}{.}99$ -$03^{\circ}03'55\overset{''}{.}4$, with a 90 per cent confidence error radius of 2 arcsec; Mereminskiy et al. 2019).

Analysis of the 2019 outburst of EXO 1846−031 has already been performed, showing: (i) Type-C QPOs in *NICER* (Bult et al. 2019) and *Insight-HXMT* (Liu et al. 2021) data; (ii) a characteristic HID to that of a BHXB (Liu et al. 2021); (iii) an ionized disc wind with a velocity up to 0.06*c* in the *Insight-HXMT* data (Wang et al. 2021); (iv) Draghis et al. (2020) argue that EXO 1846−031 is a BH with a maximal spin parameter at disc inclination of $\theta = 73^{\circ}$, though this inclination is disputed by Wang et al. (2021) who use the same data and prefer $\theta = 40^{\circ}$; (v) a compact radio source early in the outburst favoured a BH primary, as EXO 1846−031 would need to be closer than 3.7 kpc to be consistent with the brightest detections of neutron stars (Miller-Jones et al. 2019). All of the literature arguments point toward a BH nature for the compact object in EXO 1846−031, though a NS cannot be ruled out as we still lack a dynamical mass measurement.

Following the multi-wavelength reports of renewed activity of EXO 1846−031, we triggered observations (Williams et al. 2019) with the MeerKAT telescope as part of the ThunderKAT[1] Large Survey Project (Fender et al. 2016), as well as observations with the Arcminute Microkelvin Imager Large Array (AMI-LA, Zwart et al. 2008; Hickish et al. 2018) as part of a long-term program to follow up astrophysical radio transients (PI: Fender). We also acquired Karl G. Jansky Very Large Array (VLA) observations (PIs: Miller-Jones, Neilsen) throughout the outburst. Alongside these observations, we

---

[1] The **hun**t for **d**ynamic and **e**xplosive **r**adio transients with Meer**KAT**: http://www.thunderkat.uct.ac.za/

Table 1. Radio data for EXO 1846−031 for VLA. In all cases, the top row for a given date is the result for the lower frequency band and the bottom row is the result for the higher frequency band. Where a single value is given, this corresponds to the full bandwidth result. The columns in the table are as follows: (1) the start date and time in UTC for the observation; (2) the central MJD for the on source scan; (3) the central frequency of the sub-bands; (4) the brightness for each sub-band obtained from CASA fitting procedures described in Section 2.1 in mJy beam^{-1}; (5) integrated flux density in mJy for the full bandwidth of the given observation; (6) the rms noise level obtained in a region near to the source for the full band-width in μJy beam^{-1} and used as the rms level in Fig. 4; (7) the synthesized beam size in arcsec^2 for the full bandwidth image; (8) the position angle in degrees east of north for the full bandwidth image; (9) Right Ascension (top row) and associated error (bottom row) obtained from the `imfit` procedure; (10) Declination (top row) and associated error (bottom row) obtained from the `imfit` procedure. The flux densities listed in this table include a 10 per cent calibration error added in quadrature (see Section 2.1). The positional errors represent 10 per cent of the synthesized beam added in quadrature to the statistical fitting error.

Start date + Time (1)	Central MJD (2)	Freq. (GHz) (3)	Peak brightness (mJy beam^{-1}) (4)	Integrated flux (mJy) (5)	RMS noise (μJy beam^{-1}). (6)	Beam arcsec^2 (7)	P.A. ° (8)	Right Asc. + err. (9)	Declination + err. (10)
				Central component					
2019-08-01	58696.199	5.25	2.5 ± 0.3	2.5 ± 0.3	50	0.35 × 0.27	−3.1	18:49:17.047	−03:03:55.24
04:45:55		7.45	2.4 ± 0.3					$\pm 0^{\mathrm{s}}.003$	$\pm 0''.04$
2019-Aug-03	58698.107	5.25	5.9 ± 0.6	6.0 ± 0.6	35	0.43 × 0.26	−36.0	18:49:17.047	−03:03:55.25
02:34:21		7.45	6.1 ± 0.6					$\pm 0^{\mathrm{s}}.003$	$\pm 0''.04$
2019-Aug-14	58709.330	4.70	2.9 ± 0.3	2.7 ± 0.3	42	0.47 × 0.27	60.5	18:49:17.056	−03:03:55.27
07:55:48		7.40	1.5 ± 0.2					$\pm 0^{\mathrm{s}}.003$	$\pm 0''.05$
2019-Aug-28	58723.147	5.00	1.14 ± 0.10	1.11 ± 0.11	10	0.33 × 0.25	2.0	18:49:17.048	−03:03:55.26
03:31:20		7.00	0.95 ± 0.10					$\pm 0^{\mathrm{s}}.002$	$\pm 0''.03$
2019-Sep-20	58746.082	5.00	11.8 ± 1.2	15.6 ± 1.6	42	0.34 × 0.28	119.9	18:49:17.048	−03:03:55.28
01:57:54		7.00	9.5 ± 1.0					$\pm 0^{\mathrm{s}}.002$	$\pm 0''.03$
2019-Oct-20	58776.012	5.00	0.23 ± 0.02	0.31 ± 0.03	8	0.37 × 0.26	−49.0	18:49:17.045	−03:03:55.27
00:17:54		7.00	0.15 ± 0.02					$\pm 0^{\mathrm{s}}.004$	$\pm 0''.02$
				Second component					
2019-Oct-20	58776.012	5.00	0.16 ± 0.02	0.15 ± 0.02	8	0.37 × 0.26	−49.0	18:49:17.103	−03:03:55.37
00:17:54		7.00	0.10 ± 0.02					$\pm 0^{\mathrm{s}}.004$	$\pm 0''.02$

triggered an X-ray monitoring program with *Swift* to follow the new outburst in the X-ray waveband. This paper is structured as follows: in Section 2, we describe our observations and data reduction in Section 3, we present our results and discuss their implications in Section 4, and finally we summarize our conclusions in Section 5.

2 OBSERVATIONS AND DATA REDUCTION

2.1 Radio data of the 2019 outburst

2.1.1 *Karl G. Jansky VLA data*

Observations of EXO 1846−031 were performed with the Karl G. Jansky Very Large Array (VLA). The first observation was obtained on MJD 58696.199 and showed integrated flux densities of 2.54 ± 0.03 mJy and 2.42 ± 0.03 mJy at 5.25 and 7.45 GHz, respectively (Miller-Jones et al. 2019). A subsequent observation (PI: Miller-Jones, 19A-217) was made two days later (MJD 58698.107). Both of these observations used the same 8-bit correlator set-up: 2 × basebands centred at 5.25 and 7.45 GHz, each with eight spectral windows and a bandwidth of ∼1 GHz. These observations used 3C 286 as the flux calibrator and included three minutes of on-source time, as well as J1832−1035 as the phase calibrator. Four further observations (PI: Neilsen, SK0577) were obtained on MJD 58709.330, 58723.147, 58746.082, and 58776.012. All four observations were also performed in C band (6 GHz), but in slightly different correlator configurations to the 19A-217 observations. The first observation (MJD 58709.330) used two 8-bit sub-bands both of ∼1 GHz in bandwidth and eight spectral windows, centred at 4.7 and 7.4 GHz, used 3C 48 as the flux calibrator and included 85 min of on source time. The other three observations used two 3-bit basebands centred at 4.9 and 7 GHz, each with a bandwidth of ∼2 GHz, 16 spectral windows in each baseband and included 75 min of on-source time with 3C 286 as the flux calibrator and J1832−1035 as the phase calibrator. All six observations were made whilst the VLA was in A-configuration with baselines up to 36 km, yielding <0.5 arcsec angular resolution.

We downloaded the data from the VLA Archive[2] and performed initial calibration procedures using the VLA CASA pipeline version 5.6.3 (McMullin et al. 2007). After manual excision of some radio frequency interference (RFI), removal of bad antennas, we re-ran the pipeline. After final inspection of the data, we split the target field from the data and averaged the visibilities to 10 s to speed up the imaging process. We used `tclean` in CASA to make initial images with an image size of 300 × 300 pixels, a Nyquist sampled cell size between 0.04 and 0.05 arcsec, depending on the observation and Briggs weighting with a robust parameter of 0.5. A further image with a robust parameter of −1 was made to highlight compact structures. We also performed additional imaging runs in both sub-bands for all observations, so that a two-point radio spectral index could be estimated in the VLA data (see Section 2.2). We used `imfit` to extract flux densities and fold in a conservative 10 per cent flux calibration error[3] to take account of the varying flux calibrator used. Positional uncertainties of the VLA are estimated to be 10 per cent the synthesized beam, which we fold into the statistical fit errors in quadrature. Positions and source parameters are reported in Table 1. The final observation shows two clear components, which are reported separately in Table 1.

---

[2] https://data.nrao.edu/portal/

[3] 3C 48 has been varying since 2018, see: https://science.nrao.edu/facilities/vla/docs/manuals/oss/performance/fdscale

Table 2. Radio data for EXO 1846−031 for MeerKAT. The columns in the table are as follows: (1) the central MJD for the on source scan; (2) the peak brightness obtained from CASA fitting procedures described in Section 2.1 in mJy beam^{-1}; (3) the integrated flux density in mJy; (4) the rms noise level obtained in a region near to the source; (5) the synthesized beam in units of arcseconds squared and the position angle in units of degrees east of north. Upper limits are denoted with '<' and are given at the 3 × rms-noise level.

Central MJD (1)	Peak brightness (mJy beam^{-1}) (2)	Int. flux density (mJy) (3)	RMS noise μJy beam^{-1} (4)	Beam Size / P.A. arcsec^2 / ° (5)
58699.839	6.7 ± 0.7	6.9 ± 0.7	121	8.08 × 5.33 / −35.32
58705.803	30.4 ± 3.1	30.8 ± 3.1	91	8.07 × 5.56 / −38.39
58711.904	12.3 ± 1.2	12.4 ± 1.3	69	7.11 × 7.08 / −10.3
58718.695	5.4 ± 0.5	5.4 ± 0.6	69	8.46 × 6.69 / −61.19
58726.779	18.1 ± 1.8	18.2 ± 1.8	67	7.19 × 5.38 / −26.78
58733.692	34.8 ± 3.5	34.9 ± 3.5	84	8.34 × 5.82 / −44.78
58740.782	32.3 ± 3.2	32.5 ± 3.3	67	6.73 × 5.80 / −28.2
58747.654	21.4 ± 2.1	21.6 ± 2.2	80	8.27 × 5.69 / −45.02
58755.666	8.4 ± 0.9	8.6 ± 0.9	98	7.61 × 5.37 / −34.91
58762.684	3.7 ± 0.4	3.7 ± 0.4	73	7.89 × 5.42 / −34.9
58768.762	2.0 ± 0.2	2.1 ± 0.2	102	8.33 × 6.37 / −71.29
58775.646	1.5 ± 0.2	1.5 ± 0.2	89	7.47 × 5.55 / −32.26
58782.639	0.9 ± 0.1	1.3 ± 0.2	79	6.94 × 5.42 / −22.03
58788.720	0.5 ± 0.1	1.0 ± 0.3	104	7.62 × 6.64 / −38.73
58797.445	0.4 ± 0.1	0.7 ± 0.2	64	9.01 × 6.85 / 75.05
58804.439	0.4 ± 0.1	0.4 ± 0.1	73	8.24 × 6.98 / 83.76
58811.381	0.5 ± 0.1	0.5 ± 0.1	88	12.04 × 6.75 / 75.9
58817.486	–	<0.2	58	7.72 × 5.41 / −38.89
58824.359	0.7 ± 0.1	1.0 ± 0.2	67	10.37 × 6.52 / 64
58832.427	0.7 ± 0.1	0.8 ± 0.1	64	8.32 × 5.83 / −42.3
58837.469	–	<0.2	75	7.42 × 5.51 / −27.84
58845.312	–	<0.2	68	10.36 × 6.57 / 57.48
58851.438	–	<0.2	77	6.73 × 5.88 / −18.56
58900.274	–	<0.2	69	7.50 × 5.50 / −34.15
58949.314	–	<0.2	78	9.62 × 6.41 / −47.41

2.1.2 *MeerKAT data*

ThunderKAT observations of EXO 1846−031 began on 2019 August 04 (MJD 58699) and continued with approximately weekly cadence until 2020 January 03 (MJD 58851). An additional two observations were performed on 2020 February 21 (MJD 58900) and 2020 April 10 (MJD 58949). In total, we obtained 25 epochs, all of which are listed in Table 2, along with key observation properties. All MeerKAT observations were performed at a central frequency of 1.284 GHz with a bandwidth of 856 MHz, an integration time of 8 s, and consisted of one 15 minute scan of EXO 1846−031, bracketed by two minute scans of the secondary calibrator (PKS J1911−2006). Each observation included a scan of PKS J1939−6342 as the primary calibrator, to set the band pass and flux scale. Depending on the elevation of EXO 1846−031, each observation resulted in a angular resolution of 6–12 arcsec.

The data were calibrated using CASA Version 5.6.2, within the OXKAT reduction package[4] (Heywood 2020). We made *a priori* excision of RFI[5] and then split the data into eight spectral windows. The delay band pass and gain calibrations were calculated on the primary calibrator field and then applied to the secondary calibrator field. We accounted for the spectral index of the secondary calibrator and applied the solutions on to the target fields. Finally, we performed some additional flagging of RFI on the target fields before imaging. Imaging of the target field was performed using version 2.9.0 of WSCLEAN (Offringa et al. 2014; Offringa & Smirnov 2017), using a threshold mask generated from the data. Due to a large amount of bright diffuse structure in the ∼2° square target field, the median rms noise threshold achieved was ∼70 μJy beam^{-1}. For imaging, we used a pixel size of 1.1 arcsec and used a Briggs weighting with a robust parameter of −0.85. A single round of phase-only self-calibration was performed with a 64 s solution interval. We used the CASA task `imfit` to extract source positions and fluxes, folding a 10 per cent flux calibration uncertainty due to underlying systematic variations in the data (Driessen et al. 2020) in quadrature into our flux density values, which we report in Table 2. We also made images in each sub-band and performed the same fitting analysis for each epoch, which allowed us to obtain in-band spectral indices for EXO 1846−031 (see Section 2.2).

2.1.3 *AMI-LA data*

AMI-LA observations began on 2019 August 06 (MJD 58701) and continued approximately daily until 2019 October 07 (MJD 58763), occasionally missing some days due to operational issues such as high winds. The early observations were often less than two hours in duration. After the initial pseudo-daily monitoring, EXO 1846−031 was observed approximately weekly, often within 1−2 days of the MeerKAT observations to obtain bichromatic quasi-simultaneous radio data. The longest observation during this phase was four hours. Observations ceased on 2020 March 14 (MJD 58922) due to the instrument shutdown caused by the COVID-19 pandemic.

All AMI-LA observations were performed at a central frequency of 15.5 GHz with a bandwidth of 5 GHz (Zwart et al. 2008; Hickish et al. 2018). The maximum baseline length of AMI-LA is ∼110 m, leading to angular resolutions of approximately 30 arcsec, though the southern nature of EXO 1846−031 leads to a significantly elongated north–south major axis (up to 50 arcsec). All observations used a standard phase referencing technique with 10 min scans on the target source interleaved with 100 s scans of the phase calibrator source NVSS J185146+003532. Daily observations of the flux calibrator 3C 286 were used to bootstrap the flux density scale. We estimated that the flux calibration error was 8 per cent from the flux densities of the phase calibrator, which we fold in quadrature into our fluxes. The AMI-LA campaign is summarized in Table 3. Two observations obtained on 2019 September 30 and 2020 February 27 are included, but due to heavy rain and snow respectively, the instrument sensitivity is severely affected.

To calibrate the data, we used a custom reduction package `REDUCE_DC` (Davies et al. 2009; Perrott et al. 2013, 2015) and then proceeded to image the data using the Common Astronomical Software Applications CASA software (McMullin et al. 2007) task `clean`, restricting the *uv*-range to $\gtrsim 1400\lambda$ to remove the contribution of a diffuse source near to the phase centre. The CASA task `imfit` yielded flux densities, which are reported in Table 3.

2.2 Radio spectral indices

The radio spectral index, α, is a useful diagnostic for understanding the radio emission mechanism throughout the outburst (see Section 1). It is preferable to calculate a spectral index across a wider band, e.g. between AMI-LA (15.5 GHz) and MeerKAT

---

[4] https://github.com/IanHeywood/oxkat

[5] A combination of manual flags from known areas of RFI in the MeerKAT band plus automated identification and removal of RFI were used.

Table 3. Radio data for EXO 1846−031 for AMI-LA. (1) shows the central MJD of the observation, which is used in the figures in this work; (2) shows the total time on source in hours; (3) reports the peak brightness in mJy beam^{-1} with the 8 per cent calibration added in quadrature (see Section 2.1); (4) shows the rms noise level in an off-source region near the phase centre of the image. The observations marked with an '∗' are severely affected by adverse weather conditions. The '†' indicates an observation where significant flagging of one half of the band was performed due to poor rain gauge data, making it impossible to produce a spectral index across the band, as shown in Table 4.

Central MJD (1)	Obs. dur. (h) (2)	Peak brightness (mJy beam^{-1}) (3)	RMS noise (mJy beam^{-1}) (4)
58701.841	0.4	5.9 ± 0.5	0.86†
58702.876	1.5	17.4 ± 1.4	0.33
58703.905	2	5.5 ± 0.4	0.22
58706.906	2	2.5 ± 0.3	0.26†
58707.857	1	1.5 ± 0.2	0.29
58708.867	1	2.3 ± 0.2	0.25
58709.876	1	4.0 ± 0.3	0.18
58710.925	2	2.8 ± 0.3	0.43
58711.824	1	3.0 ± 0.3	0.35
58712.931	0.3	2.3 ± 0.3	0.43
58713.856	2	1.8 ± 0.1	0.23†
58714.907	1	1.7 ± 0.1	0.26
58715.865	2	1.3 ± 0.2	0.21
58717.828	2	5.3 ± 0.4	0.24
58719.816	1	<3.6	1.25
58724.811	2	4.7 ± 0.4	0.27
58726.893	1	6.4 ± 0.5	0.27
58728.841	2	18.5 ± 1.5	0.14
58729.791	2	18.6 ± 1.5	0.22
58730.811	2	22.9 ± 1.8	0.17
58731.843	1	21.8 ± 1.7	0.24
58733.869	0.4	15.3 ± 1.2	0.31
58734.839	1	16.8 ± 1.3	0.22
58735.887	0.4	18.0 ± 1.5	0.45
58738.836	1	22.7 ± 1.8	0.29
58739.730	0.4	11.8 ± 1.0	0.55
58740.878	0.25	15.0 ± 1.2	0.55
58741.800	0.4	13.5 ± 1.1	0.71
58742.799	1	12.6 ± 1.0	0.21
58744.791	1	11.9 ± 1.0	0.31
58745.790	1	10.3 ± 0.8	0.36
58747.785	1	10.2 ± 0.8	0.35
58749.770	1	11.2 ± 0.9	0.32
58750.811	0.6	9.5 ± 0.8	0.44
58751.816	1	6.7 ± 0.6	0.30
58752.794	1	4.3 ± 0.4	0.22
58756.824∗	0.2	<7.1	2.35
58758.762	2	1.7 ± 0.2	0.19
58759.729	2	1.3 ± 0.1	0.21†
58762.753	3.4	1.0 ± 0.1	0.21
58763.738	4	1.5 ± 0.1	0.14
58770.719	4	<0.42	0.14
58777.699	4	<0.54	0.18
58785.678	4	<0.51	0.17
58787.662	3	<0.42	0.14
58791.661	4	<0.42	0.14
58796.608	2	<0.57	0.19
58803.630	4	<0.33	0.11
58810.611	4	<0.51	0.17
58817.592	4	<0.54	0.18
58824.573	4	<0.42	0.14
58831.517	2.25	<0.57	0.19
58838.534	4	<0.48	0.16
58845.515	4	<0.51	0.17
58852.496	4	<0.39	0.13
58859.434	2	<0.45	0.15
58866.460	4	<0.51	0.17
58873.439	4	<0.48	0.16
58881.417	4	<0.84	0.28
58887.401	4	<1.05	0.35
58899.320	1.35	<0.93	0.31
58906.283∗	0.8	<2.40	0.80
58915.324	4	<0.69	0.23
58922.305	4	<0.63	0.21

(1.3 GHz). However, the fluxes clearly vary on a day-to-day time-scale, so simultaneity (i.e. <1 day difference) of data from different arrays is necessary to obtain reliable measurements of the spectral index. This was only possible on six occasions with AMI-LA and MeerKAT detections and five others when AMI-LA could provide an upper limit. Similarly, we were able to obtain a VLA/AMI-LA radio spectral index on two occasions and one VLA/MeerKAT radio spectral index. To supplement these radio spectral indices, we also calculated in-band spectra for MeerKAT, AMI-LA, and VLA. All of these radio spectral indices are tabulated in Table 4. For the MeerKAT data, we made an image for each of the eight spectral windows and fit a point source for EXO 1846−031 in each band for each epoch folding in the flux density bootstrapping uncertainty. We fit a radio spectral index taking into account upper limits in spectral windows, where the source was undetected with the LINMIX package (Kelly 2007). The median value from the LINMIX fitting plus the 16th and 84th quartiles are reported as the spectral indices and errors. For the AMI-LA and VLA in-band spectra, we split the band into a higher and lower frequency band, and imaged each of these separately. We fit EXO 1846−031 in each band and fold in uncertainties in the flux density into the calculation of the spectral index (Espinasse & Fender 2018). All of our radio light curves and spectral indices are shown in the first and second panels of Fig. 1, respectively.

2.3 X-ray data of the 2019 outburst

2.3.1 Swift

In order to track the outburst in X-rays, we used a combination of instruments on board *Swift*. To measure the day-to-day flux variability, we obtained data from the *Burst Alert Telescope (BAT)*[6] which probes the 'hard' X-ray energies, from 15–50 keV.

Observations were triggered as part of the ThunderKAT *Swift/XRT* follow-up programme (PI: Motta), and obtained approximately every three days. The observations were made in window timing mode. Data were reduced using the *Swift/XRT* product generator online reduction pipeline (Evans et al. 2007, 2009)[7] and downloaded for further analysis. The online reduction pipeline performs a standard analysis of XRT data and corrects for pile-up. The 0.6−10.0 keV energy band data were loaded into XSPEC 12.10.1 (Arnaud 1996) and fitted with three models: (i) an absorbed power law (TBFEO ×

---

[6] Data is publicly available here: https://swift.gsfc.nasa.gov/results/transients/weak/EXO1846-031.lc.txt

[7] https://www.swift.ac.uk/user_objects/

Table 4. Table of *quasi-simultaneous* spectral indices. Quasi-simultaneity refers to observations observed within 24 hours of one another, where there is no large day-to-day variability in the radio light curves (see Section 2.2 for details). The table lists the following: (1) the MJD (see notes below); (2) the MeerKAT (1.28 GHz) in-band spectral index; (3) the AMI-LA (15.5 GHz) in-band spectral index; (4) the VLA (∼5.5 GHz) in-band spectral index; (5) the spectral index calculated from the AMI-LA and MeerKAT data; (6) the spectral index calculated from the VLA and AMI-LA; (7) the spectral index calculated from the VLA and MeerKAT data. The MJD date refers to one of the arrays listed as 'M' for MeerKAT, 'A' for AMI-LA and 'V' for VLA. The first preference is to use the AMI-LA date, followed by the VLA date and finally the MeerKAT date. For MJD 58776.012, the VLA detection clearly shows two distinct sources (see Section 4.4). For this date, we provide a MeerKAT in-band spectral index which includes both sources (core is unmarked, jet component marked with a '∗'), as well as VLA spectra for each component separately. For the VLA/MeerKAT spectral index, we use the integrated flux densities of both components in the VLA data as the flux density value to compare to the unresolved point source flux density values in the MeerKAT data.

MJD (1)	MeerKAT in-band (2)	AMI-LA in-band (3)	VLA in-band (4)	AMI-LA/ MeerKAT (5)	VLA/ AMI-LA (6)	VLA/ MeerKAT (7)
58696.199$^{\rm V}$	–	–	−0.1 ± 0.4	–	–	–
58698.107$^{\rm V}$	–	–	0.1 ± 0.4	–	–	–
58699.839$^{\rm M}$	0.1 ± 0.2	–	–	–	–	–
58702.876$^{\rm A}$	–	−0.7 ± 0.7	–	–	–	–
58703.905$^{\rm A}$	–	−1.3 ± 0.8	–	–	–	–
58705.803$^{\rm M}$	−0.5 ± 0.1	–	–	–	–	–
58707.857$^{\rm A}$	–	−4.3 ± 0.9	–	–	–	–
58708.867$^{\rm A}$	–	−0.3 ± 0.9	−1.5 ± 0.3	–	−0.1 ± 0.2	–
58709.876$^{\rm A}$	–	−0.2 ± 0.8	–	–	–	–
58710.925$^{\rm A}$	–	−1.4 ± 0.8	–	–	–	–
58711.824$^{\rm A}$	−0.7 ± 0.1	−1 ± 1	–	−0.56 ± 0.05	–	–
58712.931$^{\rm A}$	–	−1.0 ± 0.9	–	–	–	–
58714.907$^{\rm A}$	–	−1.7 ± 1.3	–	–	–	–
58715.865$^{\rm A}$	–	−2.6 ± 1.3	–	–	–	–
58717.828$^{\rm A}$	–	−1.2 ± 0.7	–	–	–	–
58718.695$^{\rm M}$	−0.4 ± 0.2	–	–	–	–	–
58723.147$^{\rm V}$	–	–	−0.5 ± 0.4	–	–	–
58724.811$^{\rm A}$	–	−1.7 ± 0.8	–	–	–	–
58726.893$^{\rm A}$	−0.3 ± 0.1	−0.1 ± 0.7	–	−0.42 ± 0.05	–	–
58728.841$^{\rm A}$	–	−0.4 ± 0.7	–	–	–	–
58729.791$^{\rm A}$	–	−0.7 ± 0.7	–	–	–	–
58730.811$^{\rm A}$	–	−0.4 ± 0.7	–	–	–	–
58731.843$^{\rm A}$	–	−0.4 ± 0.7	–	–	–	–
58733.869$^{\rm A}$	−0.3 ± 0.1	−0.3 ± 0.7	–	−0.33 ± 0.05	–	–
58734.839$^{\rm A}$	–	−0.4 ± 0.7	–	–	–	–
58735.887$^{\rm A}$	–	−0.7 ± 0.7	–	–	–	–
58738.836$^{\rm A}$	–	−0.3 ± 0.7	–	–	–	–
58739.730$^{\rm A}$	–	−1.7 ± 0.8	–	–	–	–
58740.878$^{\rm A}$	−0.2 ± 0.1	−0.5 ± 0.7	–	−0.31 ± 0.05	–	–
58741.800$^{\rm A}$	–	0.5 ± 0.8	–	–	–	–
58742.799$^{\rm A}$	–	−0.5 ± 0.7	–	–	–	–
58744.791$^{\rm A}$	–	−0.3 ± 0.7	–	–	–	–
58745.790$^{\rm A}$	–	−0.5 ± 0.7	−0.7 ± 0.4	–	−0.4 ± 0.1	–
58747.785$^{\rm A}$	−0.3 ± 0.1	−0.4 ± 0.7	–	−0.30 ± 0.05	–	–
58749.770$^{\rm A}$	–	−1.8 ± 0.7	–	–	–	–
58750.811$^{\rm A}$	–	−1.0 ± 0.7	–	–	–	–
58751.816$^{\rm A}$	–	−1.0 ± 0.8	–	–	–	–
58752.794$^{\rm A}$	–	−0.2 ± 0.8	–	–	–	–
58755.666$^{\rm M}$	−0.4 ± 0.1	–	–	–	–	–
58758.762$^{\rm A}$	–	−1.7 ± 1.2	–	–	–	–
58762.753$^{\rm A}$	−0.5 ± 0.2	−0.5 ± 1.2	–	−0.49 ± 0.06	–	–
58763.738$^{\rm A}$	–	−3 ± 1	–	–	–	–
58768.762$^{\rm M}$	−1.2 ± 0.3	–	–	–	–	–
58776.012$^{\rm V}$	−1.6 ± 0.4	–	−1.3 ± 0.5	–	–	−0.8 ± 0.1
58776.012$^{{\rm V}*}$		–	−1.4 ± 0.7	–	–	
58782.639$^{\rm M}$	−0.7 ± 0.8	–	–	–	–	–
58788.720$^{\rm M}$	−0.8 ± 0.9	–	–	–	–	–
58796.608$^{\rm A}$	−1.6 ± 1.1	–	–	<0.1	–	–
58803.630$^{\rm A}$	−0.7 ± 1.0	–	–	<−0.1	–	–
58810.611$^{\rm A}$	−2 ± 1	–	–	<0.1	–	–
58824.573$^{\rm A}$	−1.6 ± 0.9	–	–	<−0.2	–	–
58831.517$^{\rm A}$	−1.5 ± 0.9	–	–	<−0.1	–	–

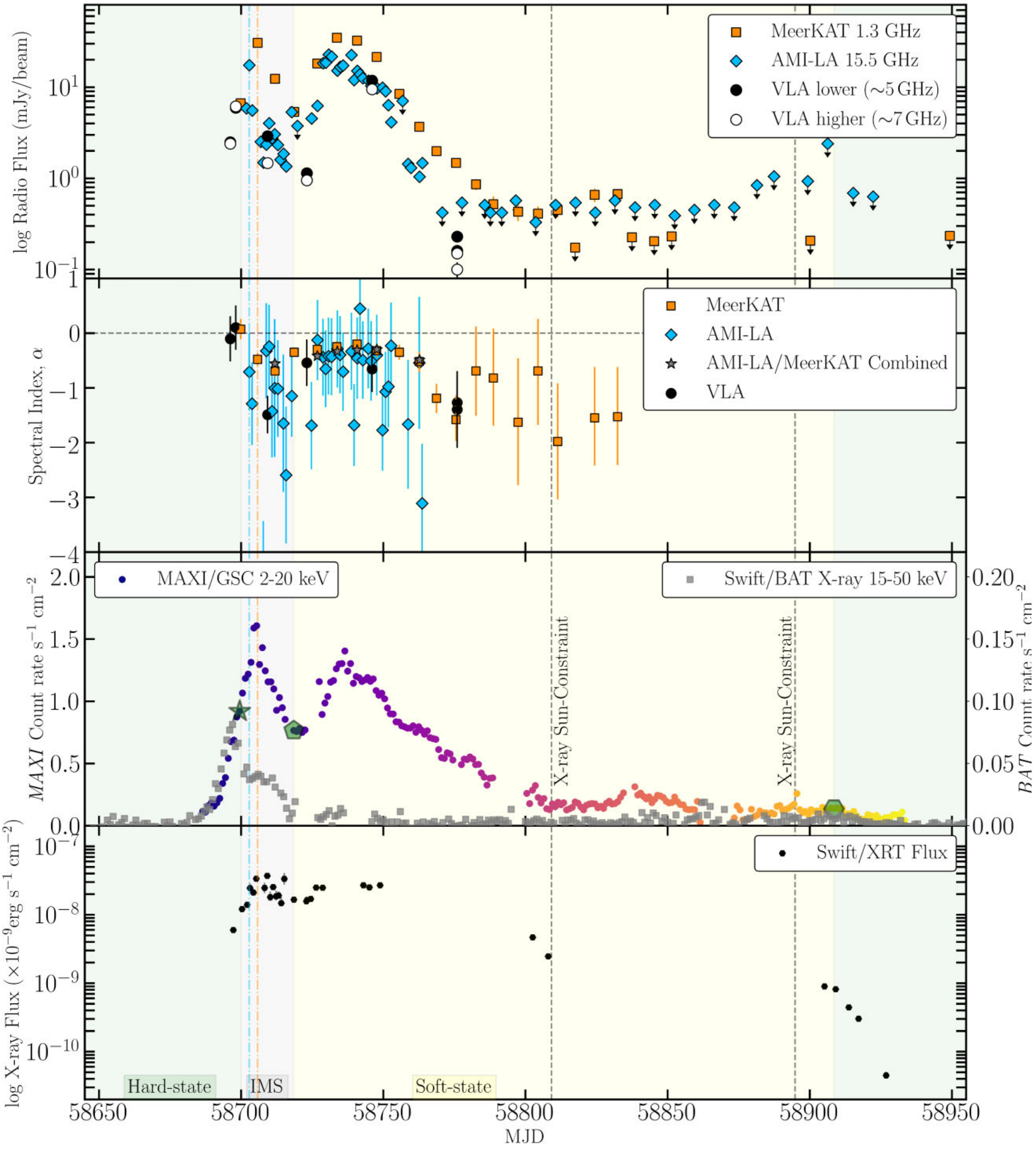

Figure 1. Radio and X-ray light curves and spectra of the 2019 outburst of the BHXB EXO 1846−031. The top panel shows the radio light curves for AMI-LA (blue diamonds), MeerKAT (orange squares) and VLA in the lower band near 5 GHz (black circles) and upper band near 7 GHz (black unfilled circles). Upper limits are denoted by downward facing arrows. The peaks in the AMI-LA and MeerKAT light curves are shown by blue or orange dashed lines in all panels, respectively. The second panel shows the in-band spectral indices for AMI-LA and MeerKAT in the same colour/marker style with grey stars denoting the AMI-LA/MeerKAT combined spectral index and the two-band VLA spectral index denoted by black circles. In both of the top two plots, the final VLA observation shows two sources (see Table 1), and we include both of these sources on this plot. The bottom two panels show the X-ray data in order: the X-ray light curve of the outburst using all-sky monitor data from *MAXI/GSC* and *Swift/BAT*; the *Swift/XRT* unabsorbed flux obtained from the X-ray spectral fits to the data. For the all-sky monitor data, the grey squares show the X-ray count rate from *Swift/BAT* in the 15–50 keV ‘hard’ band, while the coloured circles show the X-ray count rate in the *MAXI/GSC* 2–20 keV ‘soft’ band. The colour for these circles denotes the day of observing for direct comparison to Fig. 2. We represent the days where we consider the ‘hard’ state transition as a green star in the fourth panel, the first point where the source is in the ‘soft’ state as a green pentagon, and the green hexagon represents the first point where EXO 1846−031 is definitely back in the ‘hard’ state: see discussion in Section 3.1. We label these the X-ray states in the bottom panel and shade the background green, grey, or yellow for each of the X-ray states, respectively. We show with a black dashed line when EXO 1846−031 was Sun constrained for the *Swift/XRT*.

Table 5. *Swift*-XRT X-ray spectra for each epoch with fluxes and spectral parameters provided. The columns refer to: (1) The observation ID; (2) the MJD of the start of the observation; (3) the model used: TBFEO × POWERLAW denoted ‘α’, TBFEO × DISKBB denoted ‘β’, and TBFEO × (DISKBB + POWERLAW) denoted ‘δ’.; (4) the absorbing column fit in the TBFEO model × 10^{22} atoms cm^{-2}; (5) and (6) show the DISKBB $T_{\rm in}$ at inner disc radius parameter in keV and the associated normalization of this parameter; (7) and (8) show the fit power-law photon index (Γ) and associated normalization; (9) the reduced χ-squared of the fit and (10) the unabsorbed fluxes in the 1–10 keV band × 10^{-9}, in erg cm^{-2} s^{-1} obtained using the `cflux` model in XSPEC.The errors shown in this table are all at the 1σ level.

			TBFEO	DISKBB		POWERLAW		red.	Flux
ObsID (1)	MJD (2)	mod. (3)	$N_{\rm H}$ (4)	$T_{\rm in}$ (5)	norm. (6)	Phot.I. (7)	norm. (8)	χ^2 (9)	1–10 keV (10)
11500002	58697.259	α	$3.85^{+0.06}_{-0.06}$	–	–	$1.52^{+0.03}_{-0.03}$	$0.88^{+0.04}_{-0.04}$	1.0355	$5.99^{+0.06}_{0.06}$
11500003	58700.316	α	$4.27^{+0.04}_{-0.04}$	–	–	$2.09^{+0.02}_{-0.02}$	$3.6^{+0.1}_{-0.1}$	1.0197	$12.1^{+0.1}_{0.1}$
11500004	58702.094	α	$4.47^{+0.04}_{-0.04}$	–	–	$2.13^{+0.02}_{-0.02}$	$4.4^{+0.1}_{-0.1}$	1.074	$14.0^{+0.1}_{0.1}$
11500006	58703.099	δ	$3.9^{+0.3}_{-0.3}$	$1.0^{+0.1}_{-0.1}$	500^{+300}_{-300}	$2.2^{+0.3}_{-0.6}$	5^{+5}_{-4}	1.0491	24^{+4}_{-3}
11500007	58704.286	δ	$3.8^{+0.3}_{-0.2}$	$0.99^{+0.06}_{-0.05}$	800^{+200}_{-200}	$2.0^{+0.4}_{-0.8}$	2^{+4}_{-2}	1.0219	21^{+3}_{-2}
11500008	58705.288	β	$3.58^{+0.05}_{-0.05}$	$1.23^{+0.02}_{-0.02}$	870^{+60}_{-50}	–	–	1.0875	$33.6^{+0.5}_{-0.2}$
11500009	58708.214	δ	$4.2^{+0.3}_{-0.4}$	$1.1^{+0.2}_{-0.1}$	300^{+300}_{-200}	$2.8^{+0.3}_{-0.4}$	10^{+7}_{-6}	1.0093	24^{+5}_{-4}
11500010	58709.201	δ	$3.5^{+0.3}_{-0.2}$	$0.97^{+0.05}_{-0.05}$	1100^{+200}_{-300}	$1.8^{+0.6}_{-0.8}$	2^{+5}_{-2}	1.1017	26^{+3}_{-2}
11500011	58710.264	δ	$3.7^{+0.4}_{-0.3}$	$0.9^{+0.1}_{-0.1}$	700^{+400}_{-400}	$2.2^{+0.4}_{-0.7}$	4^{+6}_{-3}	0.97435	18^{+4}_{-2}
11500012	58711.262	δ	$4.1^{+0.7}_{-0.4}$	$0.9^{+0.3}_{-0.1}$	1300^{+800}_{-1100}	2^{+1}_{-2}	5^{+19}_{-5}	0.92899	88^{+3}_{-1}
11500013	58712.325	δ	$3.9^{+0.3}_{-0.4}$	$0.9^{+0.1}_{-0.1}$	600^{+300}_{-300}	$2.4^{+0.6}_{-0.6}$	6^{+5}_{-4}	1.0135	19^{+4}_{-2}
11500014	58713.184	δ	$3.7^{+0.3}_{-0.2}$	$1.04^{+0.05}_{-0.04}$	800^{+100}_{-200}	$1.9^{+0.7}_{-1.3}$	1^{+4}_{-1}	1.0405	19^{+3}_{-1}
11500015	58714.112	δ	$3.6^{+0.4}_{-0.2}$	$0.99^{+0.07}_{-0.05}$	800^{+200}_{-200}	2^{+1}_{-2}	$0.6^{+4.4}_{-0.6}$	0.91189	15^{+3}_{-1}
11500016	58715.179	δ	$4.6^{+0.3}_{-0.3}$	$1.0^{+0.2}_{-0.1}$	400^{+400}_{-300}	$3.2^{+0.3}_{-0.3}$	21^{+12}_{-10}	1.206	33^{+7}_{-6}
11500017	58718.566	β	$3.71^{+0.09}_{-0.09}$	$0.89^{+0.02}_{-0.02}$	1700^{+200}_{-200}	–	–	0.87492	$16.60^{+0.02}_{0.05}$
88981001	58722.957	β	$3.8^{+0.1}_{-0.1}$	$0.86^{+0.02}_{-0.02}$	1900^{+300}_{-300}	–	–	1.0751	$15.77^{+0.08}_{-0.07}$
88981002	58723.157	β	$3.59^{+0.08}_{-0.08}$	$0.93^{+0.02}_{-0.02}$	1500^{+100}_{-100}	–	–	1.1268	$16.38^{+0.05}_{-0.04}$
11500019	58724.481	β	$3.82^{+0.07}_{-0.07}$	$0.89^{+0.01}_{-0.01}$	1800^{+100}_{-100}	–	–	1.0124	$16.97^{+0.04}_{-0.04}$
11500020	58726.342	β	$3.68^{+0.06}_{-0.05}$	$0.91^{+0.01}_{-0.01}$	2400^{+160}_{-100}	–	–	1.0984	$25.02^{+0.05}_{-0.04}$
11500021	58728.665	β	$3.72^{+0.05}_{-0.05}$	$0.92^{+0.01}_{-0.01}$	2200^{+100}_{-100}	–	–	1.1713	$24.76^{+0.04}_{-0.04}$
11500024	58743.002	β	$3.79^{+0.08}_{-0.07}$	$0.93^{+0.01}_{-0.01}$	2400^{+200}_{-200}	–	–	1.016	$26.9^{+0.7}_{-0.6}$
11500025	58745.139	β	$3.74^{+0.06}_{-0.06}$	$0.97^{+0.01}_{-0.01}$	1800^{+100}_{-100}	–	–	1.0299	$25.1^{+0.5}_{-0.5}$
11500026	58748.839	β	$3.99^{+0.09}_{-0.09}$	$0.89^{+0.01}_{-0.01}$	2900^{+300}_{-300}	–	–	1.1024	$26.9^{+0.8}_{-0.8}$
11500028	58802.562	β	$2.8^{+0.2}_{-0.1}$	$0.88^{+0.03}_{-0.03}$	500^{+100}_{-100}	–	–	0.98232	$4.7^{+0.3}_{-0.3}$
11500029	58808.015	β	$3.6^{+0.1}_{-0.1}$	$0.76^{+0.02}_{-0.02}$	550^{+80}_{-70}	–	–	1.2375	$2.5^{+0.1}_{-0.1}$
11500030	58905.157	α	$3.4^{+0.1}_{-0.1}$	–	–	$2.15^{+0.07}_{-0.07}$	$0.29^{+0.03}_{-0.03}$	0.96611	$0.90^{+0.04}_{-0.03}$
11500031	58909.125	α	$3.5^{+0.2}_{-0.2}$	–	–	$2.20^{+0.09}_{-0.09}$	$0.28^{+0.04}_{-0.03}$	1.0726	$0.82^{+0.04}_{-0.04}$
11500032	58913.774	α	$2.8^{+0.2}_{-0.2}$	–	–	$1.9^{+0.1}_{-0.1}$	$0.11^{+0.02}_{-0.02}$	0.99995	$0.44^{+0.02}_{-0.02}$
11500033	58917.165	α	$3.0^{+0.2}_{-0.2}$	–	–	$1.7^{+0.1}_{-0.1}$	$0.06^{+0.01}_{-0.01}$	0.9711	$0.30^{+0.03}_{-0.01}$

POWERLAW), (ii) an absorbed disc model (TBFEO × DISKBB) or (iii) a combination of these two fits (TBFEO × (POWERLAW + DISKBB)). We compare these three models and choose the best fit model with physical parameters based upon the χ-squared values, but keeping the oxygen and iron abundances fixed to the defaults. Once the best fit model was obtained, absorbed, and unabsorbed fluxes were extracted using the `cflux` task in the 1.0–10.0 keV energy band, as well as the best spectral parameters and associated uncertainties. These spectral parameters and fluxes are reported in Table 5.

2.3.2 MAXI *data*

We obtained publicly available data from the Monitor of All-sky X-ray Image (*MAXI/GSC*, Matsuoka et al. 2009) for the duration of the outburst, which complemented the *Swift* XRT data. The *MAXI/GSC* data are available in different energy bands: 2–4, 4–10, 10–20, and 2–20 keV. We plot the 2–20 keV day-to-day counts in the fourth panel of Fig. 1 and plot the Hardness–Intensity Diagram (HID) of the 2019 outburst in Fig. 2. We note that the *MAXI* HID is also published in fig. 3 of Liu et al. (2021) with a detailed description of the changing X-ray classifications for the outburst using *Insight/HXMT* data.

3 RESULTS

The radio and X-ray light curves of the 2019 outburst of the BHXB candidate EXO 1846−031 are presented in Fig. 1 with a zoom in of the radio peaks in Fig. A1. The top panel shows the radio light curves for all three arrays and the second panel shows the radio spectral indices obtained from in-band and inter-array quasi-simultaneous observations (see Section 2.2). The third panel in Fig. 1 shows the X-ray monitor (*Swift/BAT* and *MAXI/GSC*) count rates, and the lower panel shows the X-ray fluxes obtained from the *Swift/XRT* X-ray spectral fitting described in Section 2.3. We

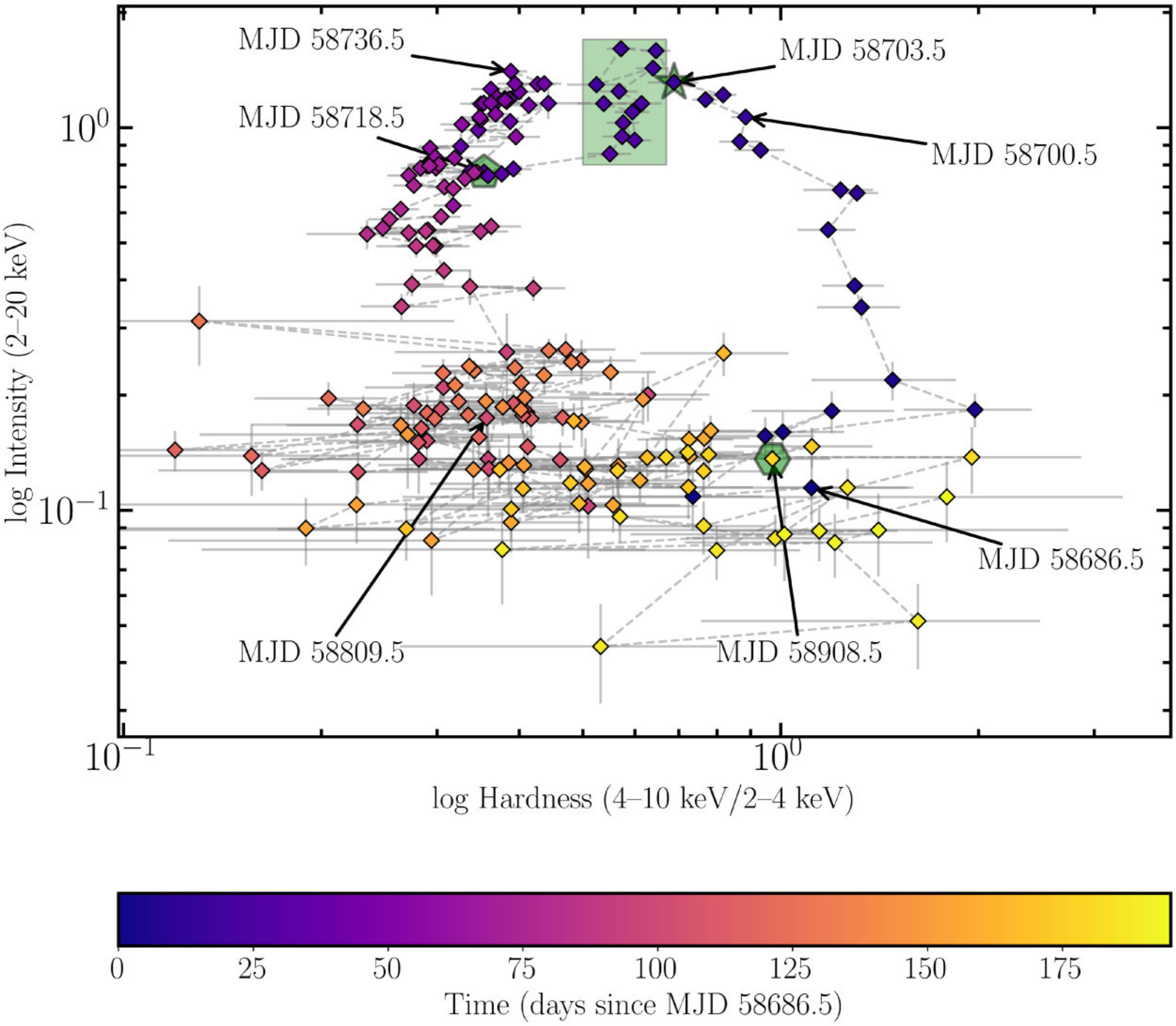

Figure 2. The *MAXI/GSC* X-ray Hardness–Intensity diagram (HID) of the 2019 outburst of EXO 1846−031, showing a characteristic q-shaped hysteresis of X-ray binaries in outburst. The data point colours correspond to the time of the observation for direct comparison with Fig. 1, normalized to a day zero of MJD 58686.5. On this plot, we label dates referring to important parts of the evolution of EXO 1846−031, moving in an anti-clockwise direction from the bottom right: MJD 58686.5 is defined as the zeroth day for the colour bar, MJD 58700.5 shows the point, which we label as the exit of the 'hard' state (see Section 3.1.1 and Fig. 3, the green star indicates MJD 58703.5, before transitioning into a 'intermediate' state (green shaded box), MJD 58718.5 (green pentagon) denotes the first date when the source was unequivocally in the 'soft' state, MJD 58736.5 is indicated as the approximate second X-ray light curve peak while in the 'soft' state, MJD 58809.5 is shown as the point where EXO 1846−031 became sun constrained and the green hexagon (MJD 58908.5) indicates when EXO 1846−031 had returned to the X-ray 'hard' state and faded into quiescence, although this exact date is unknown.

also compute a Hardness–Intensity Diagram (HID, Fig. 2), a rms–Intensity diagram (Fig. 3), and first analyse the X-ray spectral states (Section 3.1). Finally, we describe the radio behaviour and source evolution (Section 3.2), including presenting the VLA images (Fig. 4).

3.1 The X-ray spectral states and hardness–intensity diagram

Broadly, the outburst tracked the standard 'q-shaped' pattern of X-ray binaries in outburst: initially the source resided in the spectral 'hard' state (Section 3.1.1) from MJD 58687 at low fluxes, before reaching a flux peak around MJD 58700 and then softening into the 'intermediate' states (IMS) (Section 3.1.2). EXO 1846−031 remained in the IMS (MJD 58700–58717) before entering a 'soft' state for a prolonged period and gradually faded (after MJD 58717, see Section 3.1.3). Finally, at some point after MJD 58887, the source returned to the 'hard' state. We describe each of these states in detail below, including their specific X-ray behaviour.

3.1.1 The X-ray spectral 'hard' state: MJD 58687–58700

At the start of the outburst, EXO 1846−031 was in the X-ray spectral 'hard' state, as evidenced by the power-law dominated X-ray spectra and the steep-rise on the right hand side of the HID (Fig. 2). The exact end of the 'hard' state is not clear, though *Insight/HXMT* spectra indicate a transition between MJD 58697 and MJD 58703 (Liu et al. 2021).

We digitized the *Insight/HXMT* data shown in fig. 1 of Liu et al. (2021), and plotted the rms-intensity diagram (Muñoz-Darias et al. 2011) in Fig. 3 to ascertain a better transition date: the rms-intensity diagram is a good tracer of the exit from the 'hard' X-ray spectral state, and shows that the divergence from the 'hard line' may have

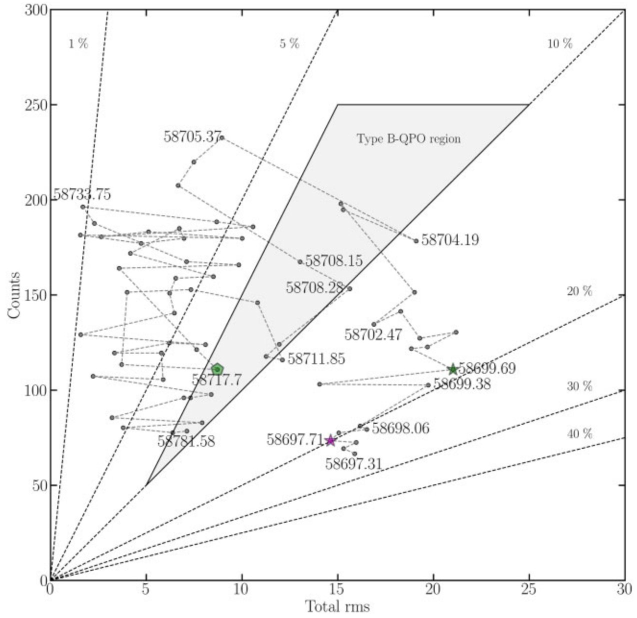

Figure 3. RMS intensity diagram for the 2019 Outburst of EXO 1846−031, using digitized *Insight/HXMT* data from Liu et al. (2021). MJDs are labelled for interesting points of the outburst. The magenta star indicates where Liu et al. (2021) suggest the source transitioned from the 'hard' to the 'hard-intermediate' state on MJD 58697. The green star (as in Fig. 1) is the last data point which is moving along the 20 per cent fractional rms variability line, and is dated on MJD 58699.7. After this date, the source clearly departs and never returns, so we consider that ∼MJD 58700 is likely the point where the state transition occurred. There is one anomalous data point on MJD 58699.5, i.e. the data point preceding the green star, but this would require a significant change in the state in less than four hours between the two data points and does not signify a state transition. The source proceeds to the 10 per cent variability line and departs across it around MJD 58704.19. The region shaded in light grey is the region identified by (Muñoz-Darias, Motta & Belloni 2011) as the region, where Type-B QPOs were seen in GX339−4. Whilst a couple of data points exist in this region, they are very short lived, often being only an hour or two long. It is therefore possible that the times for the Type-B QPO to be sampled were not available to the data in the outburst at significant signal to noise ratio, and as such explains why Type-B QPOs were not observed. This figure is replicated in Fig. A1 but zoomed in on the two peaks in the radio and X-ray light curves.

happened around MJD 58700 instead. For the purposes of this work, we consider the 'low-hard' state to finish on MJD 58700, i.e. when the source leaves the 'hard line' of the rms-intensity diagram. We label this point with a green star in panel 3 of Figs 1 and 2.

Having defined the X-ray spectral 'hard' state, i.e. up to MJD 58700, we can see that the X-ray flux in the *Swift/BAT* 15–50 keV data was decreasing after MJD 58700, but the *MAXI/GSC* 2–20 keV flux was still increasing. The two X-ray spectral fits from the *Swift/XRT* data around this time also show an increase in flux from (6–12) × 10^{-9} erg cm^{-2} s^{-1} between the MJD 58697 and MJD 58700, and are best described as an absorbed power law, although the photon index steepens between the two observations from 1.52 to 2.09.

3.1.2 The X-ray spectral 'intermediate' states: MJD 58700–58717

The sharp turn in the rms-intensity diagram after MJD 58700 indicates that EXO 1846−031 transitioned into the 'intermediate state' (IMS) on this date. We show the IMS duration in Fig. 2 as a shaded green region. During this time-frame, the *Swift/XRT* X-ray spectra change from an absorbed power-law model to an absorbed multicolour disc-blackbody plus power law model with a gradually increasing contribution to the flux from the disc component. The peak in *MAXI/GSC* is on MJD 58703, though there is some day-to-day variability in the X-ray flux extracted from the *Swift/XRT* spectra. After MJD 58703, the X-ray fluxes appear to decrease in all X-ray instruments until approximately MJD 58720.

Between MJD 58711 and MJD 58717, Liu et al. (2021) suggest that the source is in the 'soft intermediate state' (SIMS), though no Type-B QPO is observed – a common feature of the SIMS. We do not make the distinction between the 'hard' and 'soft' intermediate states, though the rms-intensity plot (Fig. 3) shows that the *Insight/HXMT* observations traverse through the region where Type-B QPOs appear briefly on several occasions. Hence it is possible that the SIMS was never fully sampled. Therefore, we consider that EXO 1846−031 was in some form of intermediate state from MJD 58700 to MJD 58717, but it is not possible to say whether the SIMS was sampled.

3.1.3 The X-ray spectral 'soft' state: after MJD 58717

After MJD 58718, the *MAXI/GSC* light curve begins to increase once more, reaching a peak around MJD 58736. However, the increase in count rate is not mirrored in the 15–50 keV *Swift/BAT* light curve. The X-ray spectra after MJD 58718 no longer require the presence of a power law to provide adequate fits to the data, which is best described by an absorbed multicolour disc model. From this point onwards, EXO 1846−031 is unequivocally in the X-ray 'soft' state, shown by the green pentagon in panel 3 of Figs 1 and 2. From MJD 58736 onwards, EXO 1846−031 starts to decrease in X-ray count rate until ∼MJD 58810. There are not many observations with *Swift/XRT* during this period, although the flux clearly decrease from ∼25 × 10^{-9} erg cm^{-2} s^{-1} around MJD 58745 to ∼3 × 10^{-9} erg cm^{-2} s^{-1} around MJD 58805.

EXO 1846−031 became the Sun-constrained for *Swift/XRT* between MJD 58809 until MJD 58894. Therefore, it is unclear when EXO 1846−031 returned to the X-ray 'hard' state. The *Swift/XRT* data from MJD 58905 onwards show a source dominated by a fading power law, so the transition back into the 'hard' state must have started before MJD 58906. We place a green hexagon at this date in the X-ray light curve (Fig. 1) and HID (Fig. 2).

3.2 Radio light curves, spectra, and evidence for jets

We now consider the radio data and compare it to the X-ray data and the state transition dates.

The first two VLA epochs were observed while the X-ray emission was still rising during the X-ray 'hard' state (Section 3.1.1), and show a compact radio source with an increasing radio flux from ∼2.5 mJy on MJD 58696 to ∼6 mJy on MJD 58698 (see top two panels in Fig. 4). While EXO 1846−031 was in the X-ray spectral 'hard' state, only one other radio observation with MeerKAT was obtained on MJD 58699.839. During this time, both the in-band VLA and MeerKAT observations show a flat ($\alpha \sim 0$) radio spectral index, as expected for sources in the 'hard' state as the radio-flux increases but the radio emission remains optically-thick.

During the IMS (Section 3.1.2, MJD 58700–58717), we observe significant changes in the AMI-LA and MeerKAT light curves and spectra, but we only have one VLA data point (third panel of Fig. 4) during this phase. The MeerKAT and AMI-LA light curves both show peaks in their light curves at a similar time to the *MAXI*

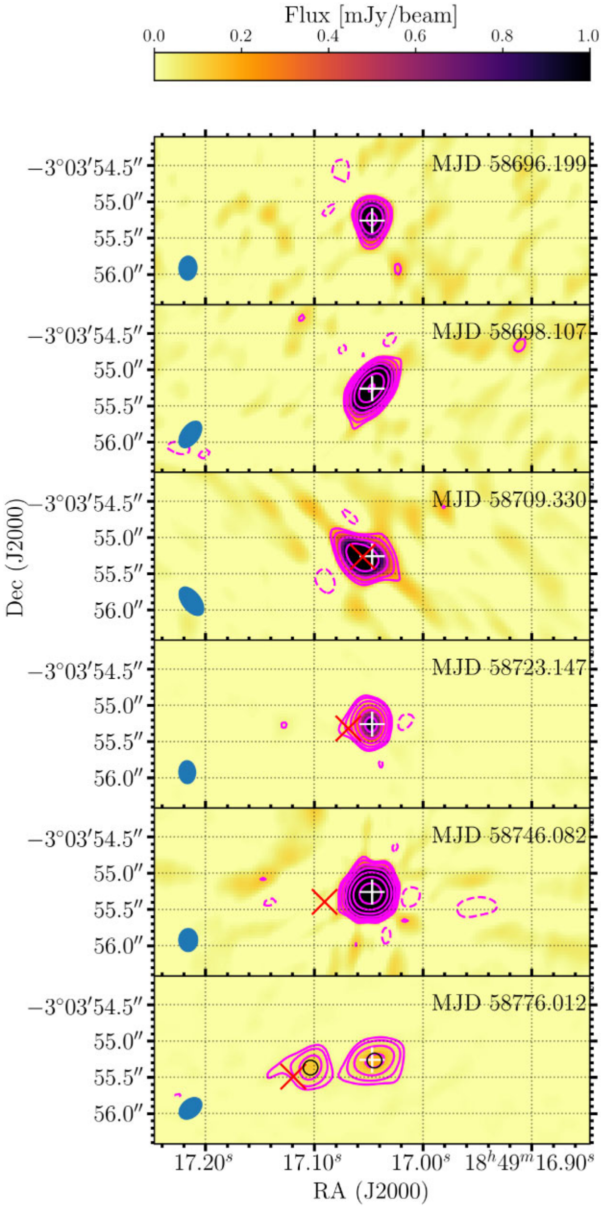

Figure 4. All six VLA epochs of the 2019 outburst of EXO 1846−031 in chronological order from top to bottom. The date of the observation is labelled in the top right hand corner of each panel: the first two observations while the source was in the X-ray 'hard' state, the third was during the 'intermediate' state, and the final three observations while the source was in the 'soft' spectral state. Each panel shows the full-band VLA dataset, but fluxes for each sub-band are given in Table 1. The background colour scale is the same for all epochs and labelled at the top of the figure, but the contour levels are set as the image rms ×−3, 3, 5, 10, 20, 40, 80, 160, 320. The image rms noise levels for the full-band width used above are shown in Table 1. The synthesized beam size and shape is shown in the bottom left-hand corner. The white 'plus' sign indicates the position of EXO 1846−031 as ascertained from the first data set and Miller-Jones et al. (2019). The red cross in panel 3 denotes the position of the first jet component, and in all later panels this red cross denotes the position where this source should reside, given a jet ejection date around MJD 58700, assuming a constant velocity. The two black circles in the final panel show the positions of the two components detected in this final epoch, showing that the eastern most component has not moved as far eastwards as expected, and the central component is located slightly westwards of the core position and therefore may be receding jet.

data (around MJD 58703), denoted in Fig. 1 with a vertical blue or orange dot–dashed line, respectively. A zoom in of this region is shown in Fig. A1. The AMI-LA data show a large day-to-day variability around this peak: on MJD 58702, the peak flux density is 17.4 ± 1.4 mJy beam^{-1}, but on MJD 59701 and 58703, it is ~5−6 mJy beam^{-1}. We label this fast rise as the 'first radio flare', which we will discuss further in Section 4.3. We split the AMI data on MJD 58702 into three parts and find no obvious intra-observation variability in this epoch. After the first peaks, all radio light curves decrease in flux density with some AMI-LA epochs around MJD 58710 decreasing to ~1 mJy beam^{-1}. Around this time, the MeerKAT flux decreases to ~5 mJy beam^{-1}. A single VLA epoch (MJD 58709.330) during this time period shows a spectrally-steep source ($\alpha = -1.5 \pm 0.3$) that has a centroid that is spatially-offset by 0.13 arcsec eastwards from the radio source identified in the first VLA epoch (see third panel in Fig. 4). We note that the error in the source position is 10 per cent the VLA synthesized beam, i.e. ~0.05 arcsec. Therefore, we made a uniform weighted image of this epoch and find a source at the same position, but with a smaller synthesized beam (0.35 × 0.27 arcsec), which provides a smaller positional uncertainty (~0.04 arcsec) and also confirms this positional movement. But, folding the positional uncertainties in quadrature from the initial BH position from Miller-Jones et al. (2009), we obtain an error of the third epoch centroid of 0.05 arcsec, which represents a $\sim 2.5\sigma$ movement eastwards. We attempted to force-fit a second component at the nominal position of the BH, but the fit was unconstrained. Thus, we consider this detection to be the first sign of a jet ejection in this system, despite the low significance. The radio spectral indices are consistent with $\alpha \lesssim 0$ throughout this period, but tend to more negative values by MJD 58717 at the end of the IMS.

As EXO 1846−031 entered the X-ray 'soft' state (~MJD 58718, see Section 3.1.3), the radio light curve mirrors the increase in the *MAXI/GSC* X-ray count rate with secondary AMI-LA/MeerKAT light curve peaks observed between MJD 58731 to MJD 58739. In particular, the AMI-LA light curve increases from 4.7 ± 0.4 on MJD 58724.811 to 22.9 ± 1.8 mJy beam^{-1} on 58730.811, which we label the 'second radio flare' (see Section 4.3). These second radio peaks are broader than the initial peak in the radio light curves. A single VLA observation on MJD 58723 during this flux density increase (panel four in Fig. 4) shows a faint (~1 mJy beam^{-1}) source that is slightly extended eastwards has a spectral index of −0.5 ± 0.4, and is spatially consistent with the initial detections of the core (see Section 4.4 for a discussion). After MJD 58740, the radio flux densities decreased across all frequencies over the following two months. The last detections were recorded on MJD 58763.738 (AMI-LA) and MJD 58832.427 (MeerKAT). Two VLA epochs during this phase (MJD 58746 and 58776, bottom two panels in Fig. 4) show resolved source structures with the sixth epoch showing a clear component 0.85 arcsec eastwards of the nominal BH position. In addition, the sixth VLA epoch showed a source offset by 0.04 arcsec westwards from the nominal BH position, but we stress that this offset is within the positional uncertainty of the initial radio detection (see discussion in Section 4.4 about the nature of this radio emission). The radio emission during this period is optically-thin, i.e. a radio spectral index <0 in all in-band observations across all observatories. After MJD 58750, the radio spectra become increasingly steeper until the source is no longer detected.

Finally, we note that around the time EXO 1846−031 returned to the X-ray 'hard' state (before MJD 58906), no quasi-simultaneous sub-mJy noise radio detections were made (see Section 3.2); the last sub-mJy noise AMI-LA observation occurred on MJD 58887.

Therefore, we suggest the return to the ‘hard’ state may have happened between MJD 58887 and MJD 58905.

4 DISCUSSION

We now discuss our results in the context of X-ray binaries, focusing on source parameters like the distance (Section 4.1), the radio:X-ray plane (Section 4.2) and the radio jets detected in the VLA data (Section 4.4).

4.1 On the distance to EXO 1846–031

Given the lack of optical counterpart (Parmar et al. 1993), the distance to EXO 1846−031 is not well constrained. The current best estimate is ∼7 kpc, but this distance is calculated assuming the peak flux in *EXOSAT* measurements corresponds to a luminosity of 10^{38} erg (Parmar et al. 1993). An accurate distance measurement is necessary for calculating the source luminosity for scaling relationships such as the radio: X-ray plane (Corbel et al. 2003; Gallo et al. 2003; Coriat et al. 2011, see Section 4.2).

A renewed search for an optical counterpart was made for the 2019 outburst, but no optical counterpart was found in the Zwicky Transient Facility (ZTF) to a limiting magnitude of $r \sim 23$ mag band (Bellm, Goldstein & Ya 2019). A search was also performed using the LCOGT network (Dave Russell, priv comm) with a limit in the $i^{'}$ band magnitude of 21.7. The large extinction in the direction of EXO 1846−031 ($N_{\mathrm{H}} \approx 3.5 \times 10^{22}$ cm^{-22}, Parmar et al. 1993), which is confirmed by our X-ray spectral fits, likely accounts for the non-detections in both the archival and new data.

We can attempt to place limits on the distance by searching for absorption in the 21 cm H I line against background sources (see e.g. Chauhan et al. 2019, 2021 for a recent examples of H I distance measurements to the XBs MAXI J1535–571 and MAXI J1348–630). We combined the MeerKAT data for the three brightest epochs ($\gtrsim$30 mJy beam^{-1}) and extracted the radio spectrum around the source position. We compared this spectrum to a nearby distant source to assess the contribution of H I in the line-of-sight to EXO 1846−031, but there was no detection of the H I line above a 3σ threshold, and so no estimate of the distance can be made from these data.

The state transition luminosity distribution of BHXBs (Maccarone 2003; Kalemci et al. 2013; Vahdat Motlagh et al. 2019) can be used as a standard method to constrain the distance in many BHXBs (Homan et al. 2005; Miller-Jones et al. 2012; Saikia et al. 2022). During the transition from the soft to the hard state, BHXBs generally have a mean Eddington luminosity fraction of 1.9 ± 0.2 per cent (Maccarone 2003), and a more conservative range of 0.3–3 per cent of Eddington luminosity (Kalemci et al. 2013), but see also the example cases of 4U 1630−47 and MAXI J1535–571, which underwent transitions at 0.008 per cent (Tomsick et al. 2014) and ∼0.002 per cent (e.g. Chauhan et al. 2019) the Eddington luminosity, respectively. For EXO 1846−031, although the exact date of the soft to the hard state transition is not certain, it appears to have happened around MJD 58905 when the source was detected post Sun-constraint. During this epoch, the 1–10 keV X-ray flux with *Swift*/XRT is 0.9×10^{-9} erg cm^{-2} s^{-1} (see Table 5). Assuming a black hole mass of 3.24 ± 0.2 M$_{\odot}$ (Strohmayer & Nicer Observatory Science Working Group 2020; Wang et al. 2021), 1.9 ± 0.2 per cent of Eddington luminosity (Maccarone 2003), and a bolometric correction factor of two relative to the *Swift*/XRT band, we obtain a distance of $\sim 6.0 \pm 0.3$ kpc for the source. For the more conservative range of 0.3–3 per cent Eddington luminosity (Kalemci et al. 2013), we constrain a distance range of 2.4–7.5 kpc.

4.2 The radio: X-ray plane

Given the lack of precise distance measurement, we attempt to reduce this uncertainty by plotting the radio and X-ray data points for the 2019 outburst on the radio:X-ray plane in Fig. 5, using three different distances: 2.4 kpc (the bottom of our distance range from Section 4.1), 4.5 kpc, and the literature value 7.0 kpc. For a given source distance, an object will move diagonally up and down the radio: X-ray plane, but as the relation between the two parameters is non-linear, an object will appear to fit the underlying distributions differently as a function of distance. We compiled all of the ‘hard’ state (before MJD 58700) quasi-simultaneous (i.e. within ∼1 day) data presented here for which the correlation holds. This limits our data set to two VLA data points (MJD 58696.199 and 58698.107) and one MeerKAT data point (MJD 58699.839).

We compare the first VLA data point to *NICER* X-ray observations from 15 h prior (Bult et al. 2019), as originally performed by Miller-Jones et al. (2019). For the second VLA data point and MeerKAT data point, we extracted the X-ray spectrum from the *MAXI/GSC* instrument in the 1–10 keV energy range using the online on-demand extraction tool,[8] fitting the spectrum using XSPEC with an absorbed power-law model and an average absorbing column from our *Swift/XRT* fits of 4×10^{22} atoms cm^{-2}. For the second VLA data point, we calculated a flux of 0.9×10^{-8} erg cm^{-2} s^{-1}. We calculate a flux of 1.2×10^{-8} erg cm^{-2} s^{-1} at the time of the MeerKAT epoch, consistent with the *Swift/XRT* fluxes. We scale the MeerKAT radio flux density to 5 GHz using the in-band spectral index ($\alpha = 0.1$).

Finally, we also plot the *Swift/XRT* data from MJD 58905 with the upper limit from our AMI-LA data on MJD 58906, as we are confident that the source had transitioned back to the ‘hard’ state at the end of the outburst by this date.

Regardless of the distance, the source appears under-luminous in the radio band to be considered one of the ‘radio-loud’ BHXBs, but a simple linear fit for the three ‘hard’ state data points gives a gradient of ∼1.0, which is in between the values for the ‘radio-quiet’ and ‘radio-loud’ populations (and the neutron stars see e.g. Coriat et al. 2011).

As for the distance, the 4.5 kpc value aligns well with the underlying ‘radio-quiet’ BH population, whereas the brightest data points for the 7 kpc literature value are X-ray brighter than many other previous XB or NS detected for any given radio luminosity. Given the paucity of data points, EXO 1846−031 could also be adequately fit at a distance of 2.4 kpc, so it is not possible to constrain the distance further than the estimate for the soft-to-hard transition noted in Section 4.1. The NSs are also plotted on this diagram, but EXO 1846−031 would need to be among one of the radio-brightest NSs detected, at any distance, given the data, including our lowest distance of 2.4 kpc. This point was also discussed by (Miller-Jones et al. 2019), who stated that the source would have to be closer than 3.7 kpc to be a NS.

Therefore, we suggest that EXO 1846−031 is a ‘radio-quiet’ BH that lies somewhere between 2.4 kpc and 7 kpc, though we prefer 4.5 kpc due to the slightly better alignment with the ‘radio-quiet’ branch objects. However, we are unable to give a more robust determination of the distance from only three data points. The exact date of transition back to the ‘hard’ state is not clear, which could help

---

[8] http://maxi.riken.jp/mxondem/

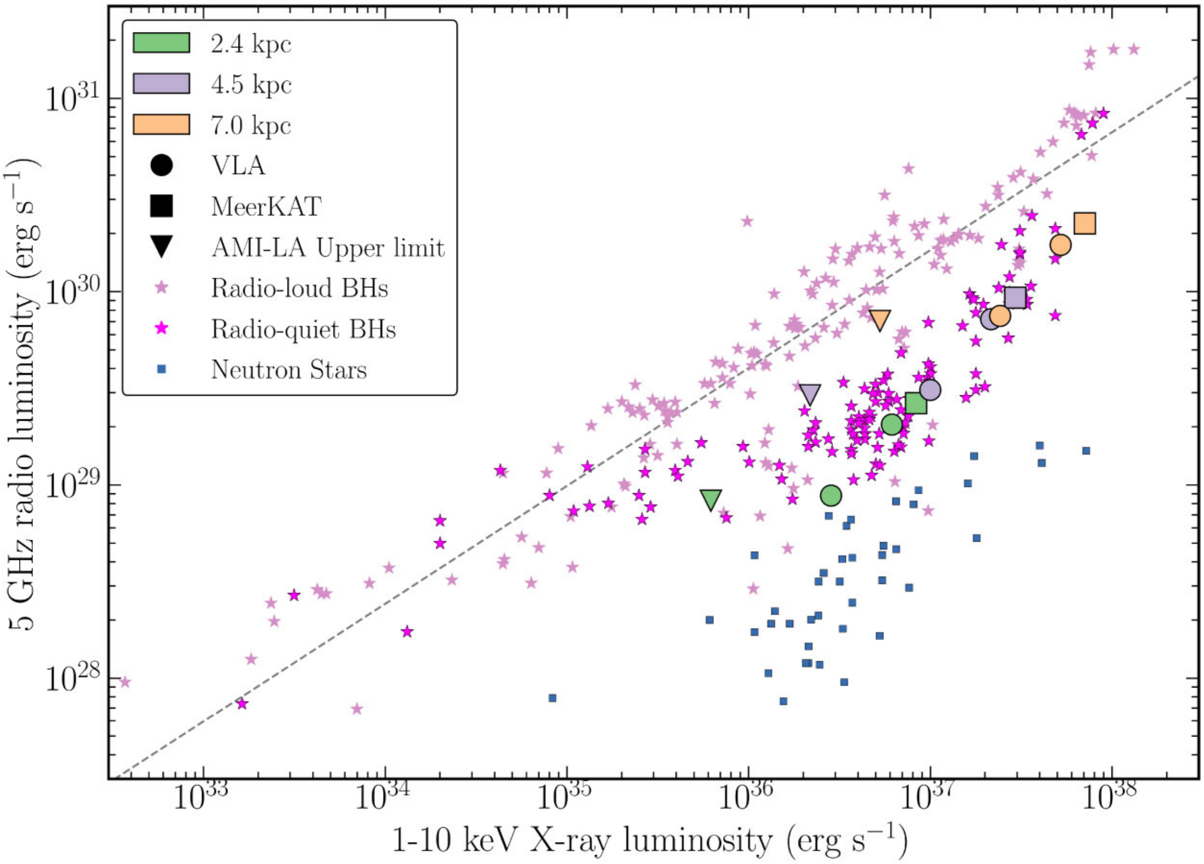

Figure 5. The radio:X-ray plane of the BHXB EXO 1846−031 for the 2019 outburst, using the VLA (circles) and MeerKAT (squares) observations with the 1–10 keV flux densities from *NICER* and *MAXI/GSC* satellites (see text). Included is an additional data point from an upper limit in the AMI-LA observations after the source had transitioned back into the 'hard' state on MJD 58905, shown as a downward triangle. Only observations with quasi-simultaneous radio and X-ray data are included in this plot. The EXO 1846−031 data points are scaled to three different distances: 2.4, 4.5, and 7.0 kpc (based off the discussion in Section 4.1). The pale and bright pink stars in the background show a compilation of 'radio-loud' and 'radio-quiet' objects from Bahramian et al. (2018), respectively. The purple squares are neutron stars from the same compilation, showing that they are unlikely to be a good fit to the EXO 1846−031 data presented here.

constrain the distance. The paucity of data points for EXO 1846−031 on the radio:X-ray plane shows further the need for rapid followup of X-ray binaries when they go into outburst and better monitoring during the hard state decay back to quiescence to better characterize this diagram.

4.3 Energy from radio flares

In Section 3.2, we identified two times when rapid increases in radio flux were observed in the AMI-LA data: flare 1 from MJD 58701.841–58702.876 where the flux increased from 5.9 ± 0.5 to 17.4 ± 1.4 mJy beam^{-1}, and flare 2 from MJD 58724.811–58730.811, where the flux increased from 4.7 ± 0.4 to 22.9 ± 1.8 mJy beam^{-1} (see Fig. A1). It is possible to calculate the energy and power imparted into this radio flare by assuming equipartition between magnetic fields and particles (Longair 2011; Fender 2006). In this case, the emission from the protons in the plasma is assumed negligible and we constrain the volume of the emitting component using the rise time of the flare e.g. equation 9.1–9.5 in Fender (2006). We use the AMI-LA central frequency of 15.5 GHz and a distance of 4.5 kpc to estimate the energies and magnetic fields.

For the first radio flare, we calculate $E_{\mathrm{min}} \sim 4 \times 10^{41}$ erg and hence a $P_{\mathrm{min}} \sim 5 \times 10^{36}$ erg s^{-1}. This power is ∼10 per cent of the X-ray luminosity on the same day and is similar to the finding for the BHXB MAXI J1348−630 (Carotenuto et al. 2021). The calculated magnetic field corresponding to the minimum energy is $B_{\mathrm{min}} \sim 14$ mG with Lorentz factor $\gamma_{\mathrm{e}} \sim 1000$. These values are similar to those found for MAXI J1348−630, ($B_{\mathrm{min}} \sim 10$ mG, $\gamma_{\mathrm{e}} \sim 5000$, Carotenuto et al. 2021), though in between the values calculated for the BHXB MAXI J1820+070 (Bright et al. 2020; Espinasse et al. 2020) ($B_{\mathrm{min}} \sim 0.2$ mG, $\gamma_{\mathrm{e}} \sim 5000$) and Cyg-X3 ($B_{\mathrm{min}} \sim 500$ mG, $\gamma_{\mathrm{e}} \sim 150$, Fender 2006), placing our values in a reasonable range compared to other BHXB flares. The same calculations for the second flare yield an order of magnitude larger minimum energy: $E_{\mathrm{min}} \sim 5 \times 10^{42}$ erg, but similar power due to the longer rise time: $P_{\mathrm{min}} \sim 9 \times 10^{36}$ erg s^{-1}. The corresponding magnetic field is $B_{\mathrm{min}} \sim 3$ mG and Lorentz factor is $\gamma_{\mathrm{e}} \sim 2200$.

4.4 The presence of discrete ejecta and XB system parameters

In Section 3.2, we showed that the third and sixth VLA panels in Fig. 4 display clear signatures of jet ejecta, which are not detected in the fourth and fifth panels. We now discuss these epochs in turn to understand the cause of these components. In order to calculate jet component speeds, we first define an origin position using the first VLA observation when EXO 1846−031 was in the 'hard' state and an unresolved point source. This position is labelled with a white 'plus' symbol in Fig. 4.

The radio source in epoch three of Fig. 4 is spectrally-steep ($\alpha = -1.5 \pm 0.3$), spatially-decoupled eastwards from the origin by 0.13 arcsec and it likely corresponds to the approaching jet ejected from the BH, though the uncertainty in this measurement is 0.05 arcsec (see Section 3.2) and we re-iterate that this component is offset by 2.5σ from the nominal BH position. If we assume that the jet ejection happened around the transition from the 'hard' state to the IMS (MJD 58700), this implies a movement of $\sim$15 mas d^{-1}. Radio jet ejections can occasionally be resolved during the hard-to-soft transition (e.g. Fender et al. 2004; Fender, Homan & Belloni 2009), so the detection of component movement is unsurprising. As we do not know the exact jet launch date, we do not attempt to put further constraints on the jet speed at this point.

The jet component in epoch three is not detected in the following two epochs, 23 and 46 days, respectively after the transition to the IMS and when the BH was in the 'soft' state. Radio emission in BHXBs during the 'soft' state is not often observed, as the steady jet emission is quenched by several orders of magnitude (Coriat et al. 2011; Russell et al. 2011, Russell et al. 2019). However, unresolved radio emission can be detected near the binary position in the case of long-lived jet ejecta, which would not be resolved in low-resolution radio images, (e.g. Bright et al. 2020). Assuming the jet continued to move at the same speed since epoch three, we would expect to detect a source $\sim$0.34 and $\sim$0.65 arcsec, respectively, offset to the east from the origin in epochs four and five (red crosses in Fig. 4). The slight eastward extension in epoch four shows that we may have detected the faint remnants of the jet which has faded rapidly. We made further images with different image weightings in order to increase the significance of such possible jet structure with no success. Similarly, we attempted a two component fit but were unable to obtain suitable fit results.

While the radio component detected in epoch five is coincident with the origin, it is resolved in the east–west direction with a source size of 246 × 123 mas and position angle of 99°. As EXO 1846−031 was clearly in the X-ray 'soft' state during epochs four and five, we suggest that these epochs show faint jet emission that has been ejected from the BH, but cannot be resolved from the origin owing to the angular resolution of the VLA data. It is plausible that further jet ejections may have occurred during the soft state, possibly after the second radio flare around MJD 58730, which confuses the localization of individual jet components. Higher resolution data would be required to resolve these components and test for multiple ejections.

The sixth VLA epoch shows two components denoted by black circles in Fig. 4, the brighter of which is consistent with, but spatially-offset from the core position westwards by 0.04 arcsec, and a fainter component 0.85 arcsec eastwards of the core position. This eastern component is most likely the re-brightening jet component first observed in the third VLA epoch, having moved further away from the core. A re-brightening may occur if the jet interacts with a denser region of the ISM. If the eastward component travelled at the same speed between the third and sixth epochs, then this corresponds to $\sim$11 mas d^{-1}. This value is similar to the initial $\sim$15 mas^{-1} observed movement estimated in epoch three, suggesting that these are the same components observed at different times. A linear fit to the separation of the eastern jet component over time would require an ejection date of $\sim$MJD 58697 when the source was clearly still in the 'hard' state as evidenced by the X-ray data, so it is possible that some deceleration may have occurred during the propagation of this jet component, which is consistent with the red cross position in Fig. 4.

The VLA data lack a clear detection of a receding jet. However, we can put limits on where we would expect it to reside by making assumptions on the distance and jet inclination. We assume a distance of 4.5 kpc, given the discussion in Section 4.1. Two inclination angles are suggested in the literature: (Draghis et al. 2020) propose a high inclination of 73° whereas (Wang et al. 2021) argue for a lower inclination of 40° from spectral fits of the same *NuSTAR* data. Empirically, 'radio-quiet' objects are found to have high-inclinations (Motta, Casella & Fender 2018), so we use the value of 73°. Given the above assumptions and from the equations in Mirabel & Rodríguez (1994), Fender (2006), the intrinsic speed of the approaching jet would be $\beta_{\rm int} \approx 0.29c$. Assuming that the receding jet was launched at the same speed in the opposite direction, it should be located 700–750 mas away from the BH.[9] As no component is detected in our VLA data at this distance, we argue that the surface brightness of the receding jet might be below our detection threshold. Using equation 2 in Mirabel & Rodríguez (1994) to estimate the flux of the receding component in our last VLA epoch,[10] we find that the source brightness would be of the order of our image r.m.s. noise level. Therefore, we would not have expected to detect this receding component at this late time. Thus, we suggest that the westward component in epoch six (MJD 58776) might be caused by secondary jet ejecta from a receding jet, but are unable to perform any further analysis.

5 CONCLUSIONS

We presented the radio and X-ray evolution of the X-ray binary (XB) EXO 1846−031 during its 2019 outburst, based on quasi-simultaneous X-ray (*Swift* and *MAXI*) and radio (1.3 GHz MeerKAT, 4–8 GHz VLA, and 15.5 GHz AMI-LA) observations. As part of the ThunderKAT X-ray binary monitoring program we observed EXO 1846−031 during 23 weekly-spaced epochs, and we obtained 19 radio detections. By studying the radio and X-ray light curves, the Hardness–Intensity Diagram (HID) and radio:X-ray plane, we showed that the evolution of EXO 1846−031 during its 2019 outburst was broadly consistent with typical 'radio-quiet' black hole X-ray binary outbursts.

The outburst began around MJD 58685 and proceeded to undertake a full hysteresis of the HID transitioning from the X-ray spectral 'hard' state on approximately MJD 58700. A radio flare was observed and peaked on MJD 58702 before the source transitioned to the X-ray 'soft' state around MJD 58718. Following a decrease in the radio and X-ray light curves, a secondary radio flare was observed and peaked at approximately MJD 58730. After several months in the 'soft' state, EXO 1846−031 transitioned back into the 'hard' state some time before MJD 58906 at low X-ray flux levels, but the exact date of transition was not covered by *Swift/XRT*.

Since a precise distance measurement of EXO 1846−031 was not available, we first calculated a distance from the soft-to-hard state transition luminosity distribution of BHXBs of 2.4–7.5 kpc (Kalemci et al. 2013). We attempted to estimate the distance from the available X-ray 'hard' state radio and X-ray data using the radio:X-ray plane. Using this method, we showed that the gradient of the radio:X-

---

[9] We note that for a different combination of assumptions, e.g. $\theta = 40°$ and $d = 7.0$ kpc, we would have still have seen a receding component >400 mas away from the original position in our final VLA epoch, which we clearly do not observe.

[10] We use a value of $k = 3$ for a discrete condensation in this calculation, and the spectral index and approaching jet flux from Tables 4 and 2, respectively.

ray correlation for EXO 1846−031 was ∼1.0 but were unable to constrain the distance estimate further; the data align best with a distance of ∼4.5 kpc, but the paucity of data points prevents any meaningful uncertainties. A BH primary is preferred to a NS in EXO 1846−031, as evidenced by the distance (Miller-Jones et al. 2019) and the trends on the radio:X-ray plane: if EXO 1846−031 is a NS, it would be one of the radio-brightest NSs to be discovered.

We estimated equipartition minimum energies of each of the observed AMI-LA radio flares to be $E_{\rm min} \sim 4 \times 10^{41}$ and 5×10^{42} erg for each flare, respectively. These values and their associated powers ($P_{\rm min} \sim 5 \times 10^{36}$ and 9×10^{36} erg, respectively) are broadly consistent with other radio jetted BHXBs in the literature, including MAXI J1348–630 (Carotenuto et al. 2021) and MAXI J1820+070 (Bright et al. 2020).

We observed steepening radio spectral indices around MJD 58750 which suggest optically-thin radio emission, possibly from unresolved radio ejecta in all three radio light curves. The VLA observations detected the presence of an eastward jet component 0.85 arcsec from the core position. We thus calculate an intrinsic jet speed of $\beta_{\rm int} = 0.29c$ for the eastward component, assuming a distance of 4.5 kpc and an inclination angle of $\theta = 73^{\circ}$, but we were unable to conclusively detect a receding jet component, and are unable to put further strong constraints on the system geometry. We suggest that the observed radio components that are consistent with the XB core position while in the soft state are from unresolved, potentially additional jet ejections; higher resolution interferometers would have been required in this instance to conclusively resolve the receding jet emission.

The ThunderKAT X-ray binary monitoring programme has been operational for three years and is continuing to detect radio jet emission and discrete radio jet ejecta from BHXB systems. Historical systems like EXO 1846−031, where previous radio detections were not possible, are potential targets for ThunderKAT and offer the chance to further understand XB jet emission in a co-ordinated framework – this work has highlighted the need for regular radio monitoring at high resolution to resolve jet emission and extract physical system parameters.

ACKNOWLEDGEMENTS

This work was supported by the Oxford Centre for Astrophysical Surveys, which is funded through generous support from The Hintze Family Charitable Foundation. JvdE is supported by a Lee Hysan Junior Research Fellowship awarded by St. Hilda’s College, Oxford. We thank the staff at the South African Radio Astronomy Observatory (SARAO) for their rapid scheduling of these observations. The MeerKAT telescope is operated by SARAO, which is a facility of the National Research Foundation, an agency of the Department of Science and Innovation. We also acknowledge the staff who operate and run the AMI-LA telescope at Lord’s Bridge, Cambridge, for the AMI-LA radio data. AMI is supported by the Universities of Cambridge and Oxford, and acknowledges support from the European Research Council under grant ERC-2012-StG-307215 LODESTONE. The National Radio Astronomy Observatory is a facility of the National Science Foundation operated under cooperative agreement by Associated Universities, Inc. We acknowledge the use of public data from the *Swift* data archive. This research has made use of MAXI data provided by RIKEN, JAXA, and the MAXI team. This research made use of APLpy, an open-source plotting package for Python (Robitaille & Bressert 2012). DRAW would like to acknowledge the help of Mark Lacy at the NRAO Help Desk for suggestions that greatly improved the VLA data calibration and imaging quality.

DATA AVAILABILITY

All of the X-ray data presented here (*Swift/XRT*, *Swift/BAT* and *MAXI/GSC*) can be downloaded from the public archives, note in the manuscript. The radio data (MeerKAT and AMI-LA) can be made available on request to the corresponding author. The VLA data is publicly available on the NRAO VLA archive.

REFERENCES

Arnaud K. A., 1996, in Jacoby G. H., Barnes J., eds, ASP Conf. Ser. Vol. 101, Astronomical Data Analysis Software and Systems V. Astron. Soc. Pac., San Francisco, 17
Bahramian A. et al., 2018, Radio/X-ray Correlation Database for X-ray Binaries. Zenodo, available at https://github.com/bersavosh/XRB-LrLx_pub
Bellm E. C., Goldstein D., Ya Y., 2019, ATel, 12991, 1
Belloni T. M., Motta S. E., 2016, in Bambi C., ed., Astrophysics and Space Science Library Vol. 440, Astrophysics of Black Holes: From Fundamental Aspects to Latest Developments. Springer-Verlag, Berlin, Heidelberg, p. 61
Belloni T. et al., 2006, MNRAS, 367, 1113
Bright J. S. et al., 2020, Nat. Astron., 4, 697
Bult P. M. et al., 2019, ATel, 12976, 1
Carotenuto F. et al., 2021, MNRAS, 504, 444
Casella P., Pe’er A., 2009, ApJ, 703, L63
Chauhan J. et al., 2019, MNRAS, 488, L129
Chauhan J. et al., 2021, MNRAS, 501, L60
Corbel S., Fender R. P., Tzioumis A. K., Nowak M., McIntyre V., Durouchoux P., Sood R., 2000, A&A, 359, 251
Corbel S., Fender R. P., Tzioumis A. K., Tomsick J. A., Orosz J. A., Miller J. M., Wijnands R., Kaaret P., 2002, Science, 298, 196
Corbel S., Nowak M. A., Fender R. P., Tzioumis A. K., Markoff S., 2003, A&A, 400, 1007
Corbel S., Fender R. P., Tomsick J. A., Tzioumis A. K., Tingay S., 2004, ApJ, 617, 1272
Corbel S., Kaaret P., Fender R. P., Tzioumis A. K., Tomsick J. A., Orosz J. A., 2005, ApJ, 632, 504
Corbel S., Koerding E., Kaaret P., 2008, MNRAS, 389, 1697
Corbel S., Coriat M., Brocksopp C., Tzioumis A. K., Fender R. P., Tomsick J. A., Buxton M. M., Bailyn C. D., 2013, MNRAS, 428, 2500
Coriat M. et al., 2011, MNRAS, 414, 677
Davies M. L. et al., 2009, MNRAS, 400, 984
Draghis P. A., Miller J. M., Cackett E. M., Kammoun E. S., Reynolds M. T., Tomsick J. A., Zoghbi A., 2020, ApJ, 900, 78
Driessen L. N. et al., 2020, MNRAS, 491, 560
Espinasse M., Fender R., 2018, MNRAS, 473, 4122
Espinasse M. et al., 2020, ApJ, 895, L31
Evans P. A. et al., 2007, A&A, 469, 379
Evans P. A. et al., 2009, MNRAS, 397, 1177
Fender R., 2006, Jets from X-ray Binaries. Cambridge Univ. Press, Cambridge, p. 381
Fender R., Belloni T., 2004, ARA&A, 42, 317
Fender R. P., Belloni T. M., Gallo E., 2004, MNRAS, 355, 1105
Fender R. P., Homan J., Belloni T. M., 2009, MNRAS, 396, 1370
Fender R. et al., 2016, Proc. Sci., MeerKAT Science: On the Pathway to the SKA. SISSA, Trieste, PoS#13
Gallo E., Fender R. P., Pooley G. G., 2003, MNRAS, 344, 60
Gallo E., Miller B. P., Fender R., 2012, MNRAS, 423, 590
Gallo E. et al., 2014, MNRAS, 445, 290
Gallo E., Degenaar N., van den Eijnden J., 2018, MNRAS, 478, L132
Gottwald M., Steinle H., Graser U., Pietsch W., 1991, A&AS, 89, 367
Hannikainen D. C., Hunstead R. W., Campbell-Wilson D., Sood R. K., 1998, A&A, 337, 460

Heywood I., 2020, Astrophysics Source Code Library, record ascl:2009.003
Hickish J. et al., 2018, MNRAS, 475, 5677
Homan J., Belloni T., 2005, Ap&SS, 300, 107
Homan J., Miller J. M., Wijnands R., van der Klis M., Belloni T., Steeghs D., Lewin W. H. G., 2005, ApJ, 623, 383
Inoue H., Nagase F., Ishida M., Sonobe T., 1994, IAU Circ., 6099, 1
Kalemci E., Dinçer T., Tomsick J. A., Buxton M. M., Bailyn C. D., Chun Y. Y., 2013, ApJ, 779, 95
Kelly B. C., 2007, ApJ, 665, 1489
Koljonen K. I. I., Russell D. M., 2019, ApJ, 871, 26
Liu H.-X. et al., 2021, Resear. Astron. Astrophysi., 21, 070
Longair M. S., 2011, High Energy Astrophysics. Cambridge Univ. Press, Cambridge
Maccarone T. J., 2003, A&A, 409, 697
Matsuoka M. et al., 2009, PASJ, 61, 999
McMullin J. P., Waters B., Schiebel D., Young W., Golap K., 2007, in Shaw R. A., Hill F., Bell D. J., eds, ASP Conf. Ser. Vol. 376, Astronomical Data Analysis Software and Systems XVI. Astron. Soc. Pac., San Francisco, 127
Mereminskiy I. A., Krivonos R. A., Medvedev P. S., Grebenev S. A., 2019, ATel, 12969, 1
Meyer-Hofmeister E., Meyer F., 2014, A&A, 562, A142
Miller-Jones J. C. A., Jonker P. G., Dhawan V., Brisken W., Rupen M. P., Nelemans G., Gallo E., 2009, ApJ, 706, L230
Miller-Jones J. C. A. et al., 2012, MNRAS, 421, 468
Miller-Jones J., Russell T., Sivakoff G., Tetarenko A., 2019, ATel, 12977, 1
Mirabel I. F., Rodríguez L. F., 1994, Nature, 371, 46
Motta S. E., Casella P., Fender R. P., 2018, MNRAS, 478, 5159
Muñoz-Darias T., Motta S., Belloni T. M., 2011, MNRAS, 410, 679
Negoro H. et al., 2019, ATel, 12968, 1
Nelson R. F., Spencer R. E., 1988, MNRAS, 234, 1105
Offringa A. R., Smirnov O., 2017, MNRAS, 471, 301
Offringa A. R. et al., 2014, MNRAS, 444, 606
Parmar A. N., White N. E., 1985, IAU Circ., 4051, 1
Parmar A. N., Angelini L., Roche P., White N. E., 1993, A&A, 279, 179
Perrott Y. C. et al., 2013, MNRAS, 429, 3330
Perrott Y. C., Scaife A. M. M., Green D. A., Grainge K. J. B., Hurley-Walker N., Jin T. Z., Rumsey C., Titterington D. J., 2015, MNRAS, 453, 1396
Plotkin R. M. et al., 2017, ApJ, 834, 104
Remillard R. A., McClintock J. E., 2006, ARA&A, 44, 49
Robitaille T., Bressert E., 2012, Astrophysics Source Code Library, record ascl:1208.017
Russell D. M., Miller-Jones J. C. A., Maccarone T. J., Yang Y. J., Fender R. P., Lewis F., 2011, ApJ, 739, L19
Russell T. D. et al., 2019, ApJ, 883, 198
Saikia P. et al., 2022, ApJ, 932, 38
Stirling A. M., Spencer R. E., de la Force C. J., Garrett M. A., Fender R. P., Ogley R. N., 2001, MNRAS, 327, 1273
Strohmayer T. E., Group Nicer Observatory Science Working, 2020, Bull. Amer. Astronom. Soc., 52, 159.02
Tomsick J. A., Yamaoka K., Corbel S., Kalemci E., Migliari S., Kaaret P., 2014, ApJ, 791, 70
Tremou E. et al., 2020, MNRAS, 493, L132
Vahdat Motlagh A., Kalemci E., Maccarone T. J., 2019, MNRAS, 485, 2744
Wang Y. et al., 2021, ApJ, 906, 11
Wenzel W., Huth H., 1985, IAU Circ., 4059, 1
Williams D., Fender R., Woudt P., Miller-Jones J., 2019, ATel, 12992, 1
Williams D. R. A. et al., 2020, MNRAS, 491, L29
Wood C. M. et al., 2021, MNRAS, 505, 3393
Zhang S. N. et al., 1994, IAU Circ., 6096, 1
Zwart J. T. L. et al., 2008, MNRAS, 391, 1545

APPENDIX A: ZOOM PLOT OF THE RADIO AND X-RAY LIGHT CURVES

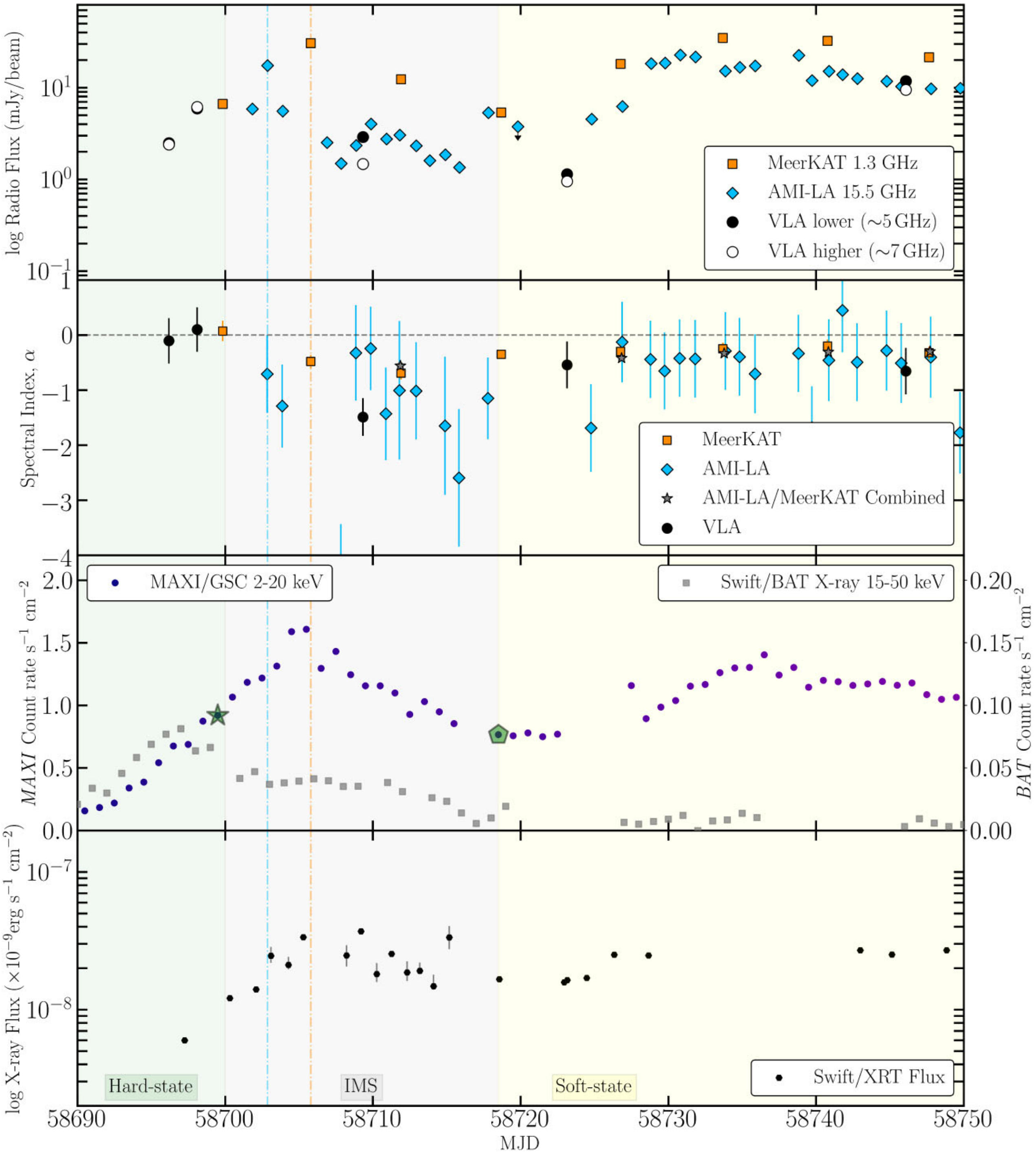

Figure A1. Radio and X-ray light curves and spectra of the 2019 outburst of the BHXB EXO 1846−031 for the region between MJD 58690 and MJD 58750. The panels are identical to Fig. 1 with minor changes to the y-axis to better represent the data: the top three panels have an identical y-axis scale to Fig. 1, but the bottom panel (*Swift/XRT* fluxes) are restricted to the range between 10^{-7}–10^{-9} erg, where Fig. 1 extended to 10^{-11} erg.

This paper has been typeset from a TEX/LATEX file prepared by the author.